C O M M U N I C A T I O N S

C O M M U N I C A T I O N S

This Journal is published two issues in a year by the Faculty of Sciences, University of Ankara. Articles and any other material published in this journal represent the opinions of the author(s) and should not be construed to reflect the opinions of the Editor(s) and the Publisher(s).

©Ankara University Press, Ankara 2021

Research Articles

DESIGN AND IMPLEMENTATION OF A LOW COST, HIGH PERFORMANCE IONIZING RADIATION SOURCE DETECTION AND SOURCE DIRECTION FINDING SYSTEM

Burak ÇUHADAROĞLU[1] and Hakkı Gökhan İLK[1]

[1]Department of Electrical and Electronics Engineering, Ankara University, Ankara, TURKEY

ABSTRACT. This study shows the design, implementation, and test results of a low-cost portable radiation-detector system relies on a directionally designed multi detector probe that works in Geiger-Müller counting mode with a single chip solution. The proposed system can perform the functions of detecting the ionizing radiation source, counting gamma and showing the direction and angle of the gamma source relative to the position of the device. The radiation direction finding (RDF) system consists of a radiation probe and electronic sections that are mounted in a metal box. The probe has a has a cast housing made of lead material and it has 8 directional slots for placing the optically isolated PIN diode arrays where each array consists of 4 parallelly connected BPW 34 PIN model diode. The lead housing also blocks incident rays from unintended directions and provides a directional sensing for PIN diodes. The metal box contains 8 low noise amplifiers and pulse shaping detector boards that are assigned to each channel of PIN diode arrays, a signal inverter board, a step-up high voltage board, a 12 V battery and a parallel processing FPGA board with an embedded VHDL software that can process all 8 channels simultaneously and execute the direction estimation algorithm. The system also has an adjustable detector bias voltage and the applied voltage can be displayed on a seven-segment display located in front of the unit so that different models of PIN diodes can be used and tested with different bias voltage levels. It also has a HMI touch screen unit and user interface for displaying the Cpm or Cps values of each channel; a 360-degree scale showing the direction of the source with its pointer and an indicator showing the direction of the source numerically in degrees. The system works as a gamma detector and the source direction can also be detected within ±45° interval. The success of system within this interval is 99.22%. The detector was tested with low to high energy gamma sources (^{241}Am, 9.761 µCi, 59.54 keV, ^{137}Cs 661, 3.7 MBq, keV and ^{60}Co, µCi, 1173 and 1332 keV) and showed good sensitivity performance level in gamma ray detection. The major

outcome of this study and the major contribution of this work to the literature is therefore is the design and production details of a hand-held detector and source direction locator prototype; which is a light, portable and compact system.

1. Introduction

Gamma radiation sources are widely used in metal-encapsulated forms for medical, industrial and research purposes and they are subject to government regulatory control for public health and security. Spent and orphan sources may be harmful to unaware people; should be immediately detected and held by the trained and equipped search teams that will provide source safe until collection and off-site transport. Moreover, other gamma ray sources that are stolen, lost, abandoned, misplaced, unknown owner sources and illegally transferred or stored, and sources intentionally obtained by terrorists also cause safety risk. For safety reasons scrap metal recycling, custom offices, border controls or Nuclear Agencies use gamma detectors for searching lost isotopes, radioactive materials or radioactive contaminations and detecting the gamma ray leakage in nuclear facilities. Remote sensing of nuclear accidents and gamma rays' arrival angle estimation is an important parameter in these radiation monitoring and detection applications. A standard radiation source searching project requires to know dose and time duration that the person will be exposed to gamma ray and a team equipped with shielded clothes and detectors and active personal dosimetry. Existing systems provide energy and pattern change in indicated values. The surveyors should detect the position of the gamma source by personal skills and estimation and this increases the exposure time and dose to be received [1]. Compton cameras, which are mostly employed in the astrophysics area, count-based systems, collimators, and coded aperture systems are the three broad categories for gamma source direction determination. Two-dimensional semiconductor Germanium Strip Detectors (GSD) are used in high energy astrophysics fields by measuring energy and position of interactions and having better energy resolution and imaging then typical germanium detectors [2]. The spatial resolution in a device with 1 cm thickness is almost 200μm and limited by strip pitch of the device and the lateral dispersion of the charge cloud after an interaction [3]. Imaging gamma-ray detectors with double-sided germanium detector sensitive polarimeters use the Compton scattering cross-angular section's dependency on polarized gamma rays and the distribution of scatter orientations within the detector and optimized Compton polarimeters give more sensitive results [4]. In addition to GSD, thick microstrip 3D multilayer detectors having the advantage of lower doppler broadening by its low Z and capable of observing three Compton scatter technique are used in high resolution position sensitive detectors with low power ASICs capable of handling large number of channels connected to the arrays of microstrip detectors were developed in Naval Research Laboratory

(NRL) [5]. The advanced gamma-ray tracking-based Compton cameras have superior sensitivity in imaging gamma-ray sources than collimator-based systems and also increase the sensitivity for finding gamma-ray sources mainly in complex radiation fields, over the other non-imaging type detectors [6]. Based on the high purity germanium (HPGe) systems, the Advanced GAmma Tracking Array (AGATA) was developed in Europe with the participation of more than 10 countries [7] and also in the USA, the Gamma Ray Energy Tracking Array (GRETA) was developed [8]. The HPGe detectors that are 100-200 highly segmented were placed in the system with a 4π geometry. By using the measured information and energy from the interaction points the paths are reconstructed by using developed reconstruction and backscattering algorithms [9]. Another suggested system is wind rose type gamma detector having dozens of scintillators and a position sensitive photo multiplier tube (PSPMTs) that could identify only lateral directions and a detector with two NaI (Tl) scintillators with a triangle shape lead shield with the disadvantage of identifying the most significant incident angle was suggested. Various types of detectors' designs including a design similar to our device design, a spherical designed honeycomb-type detector system consisting of many scintillator pieces, a PSPMT and light guides was suggested for this purpose [10]. A system with a lead shield having special shape, a NaI (Tl) scintillator with 3" x 3" dimensions and software was developed tested by rotating the shield 90 ° for 10-20 minutes and taking four measurements of energy spectra for one local position [11]. The Soft Gamma-ray Detector (SGD) is a Compton telescope developed in NeXT (Japanese future high energy astrophysics mission) that consist of a hybrid silicon and CdTe having a narrow field of view (FOV. This detector has background rejection gamma ray polarization measurement and high angular resolution capabilities by using Compton kinematics [12]. A designed gamma-ray detector for direction-finding purpose with three pieces of NaI (Tl) and CsI (Tl) scintillators and three photomultipliers; which was placed in a cylindrical housing with 120° could measure gamma ray energy and count. The incident angle was calculated by counting weight-based algorithm [13]. A similar system with the same structure having NaI (TI) scintillator system was also designed and gamma sources within 60-1250 KeV energy were measured the algorithms based on the weight of each detector counts to the total counts with $\pm 3°$ angles. The resolution was less with respect to the previous design [14]. An approach by using two measurements with segmented gamma scanner (SGS) in opposing directions were evaluated and recommended for use by waste disposal regulators for the assay of radioactive waste drums primarily composed of organic materials [15]. Another gamma vector camera (GVC) that also can measure the direction of the neutron sources by using double neutron scattering and calculating the statistical mean of the incidence direction of the scattered neutron was developed with the help of DARPA by using polystyrene fibers and observed

by CCD (charge coupled device) cameras and additional image intensifiers. The system was tested by GEANT4 simulations [16]. Another system having three NaI detector placed in a housing connected to photomultiplier tubes, ADC blocks measuring the pulse heights of each detector a low power single CMOS chip that calculates the angle of incidence by using the proposed algorithm within 5° [17]. Another three-dimensional position-sensitive semiconductor detector was developed using the generalized likelihood ratio test (GLRT). Using the combined energy and direction information from these detectors, the source-intensity test (SIT) is used to automate the detection and identification of point sources of radiation in the diffused background. SIT outperformed commercial software Genie 2000 (Canberra) [18]. A system was suggested with the three-perpendicular quadratic NaI scintillator array placed perpendicular to each other for determining the incidence angle of cosmic rays and simulations in GEANT performed small variations [19]. A circular arranged multi BGO-SiPM-panel with gamma-ray detectors that are having directional sensitivity to be used in the radiological searches for the low-altitude applications was mounted on an un-manned aerial (UASs) system and the systems signal outputs are processed by a FPGA for the estimation methods Maximum Likelihood Estimation, Matched Filtering and Weighted Symmetry for finding the direction. The minimum activity that the system can detect for a ^{137}Cs source at 1 m distance for 60 s period was measured as 1.3 μCi and direction estimation performance was calculated with 2.3° accuracy [20]. The Bayesian based algorithm was also used for localizing the orphan sources by using mobile gamma spectrometry. The HPGe detector mounted vehicle system was tested with the ^{131}I, ^{133}Ba and ^{137}Cs gamma radiation sources. The method performed estimation success for activity within 50% and location within 27% uncertainty [21]. A detector with a 0.1 L cylindrical NaI(TI) scintillator was mounted on (UASs) for gamma radiation mapping and source localization. The minimum source detectable height for UAV is almost 10 m for the ^{137}Cs test sources with 35 MBq and 350 MBq activities. The results show that UASs have advantage for hard terrain condition mapping against terrestrial robots. [22]. An alternative direction sensitive system was the rotating scatter mask (RSM) concept that uses a low-Z polyethylene mask located over a position-insensitive detector and energy spectra was recorded with accordance to the geometrically varying blocking mask while the mask rotated at a constant speed. The position dependent spectra were recorded and the detector response curves (DRCs) were constructed to be used for identifying the source direction [23]. For reducing linear dependence of DRCs' using optimization of the mask's shape geometry, three following methods were suggested: The eigenvector approach, the binary method and the modified Hadamard approach were used for the rotating encoding mask types. The Eigen and Spartan general design classes were developed to create the RSM geometries [24]. In the previous studies the Mace mask that reduces the

similarities between the modes was developed. A new design class was simulated and compared to the Mace mask design by evaluating the differentiability of directed modes using the modal assurance criterion. It has the disadvantage of a reduced field-of-view but also can decouple the source directions angular components and improves the average criterion value [25]. Another study utilized an algorithm to evaluate the List Mode Maximum Likelihood Expectation Maximization (LM-ML-EM) imaging techniques using a position-sensitive portable radiation device (COCAE). The source-to-detector distance was then determined using three distinct algorithms: a) the photo-peak count information from each detecting layer, b) the quality of the reconstructed source image, and c) the triangulation method, which was based on the photo-peak count information from each detecting layer for point-like radioactive sources located at various orientations and distances and simulation. In this study, we present a homemade portable gamma radiation detector unit that is capable of working both as a gamma counter and finding the position angle of the existing radiation source. The system consist of a designed detector probe head, electronic blocks (LNA(low noise amplifier), filters, inverter and high voltage power blocks, and FPGA boards), HMI touch screen and user interface for displaying measurements and radiation source position numerically and also by a 360 degree scale, FPGA unit and VHDL based embedded software capable of parallel processing and an algorithm for interpreting the concurrent measurements and estimating the angular position of the gamma radiation source in degree base with respect to the detectors position. It also gives quick response after powering on and provides almost $\pm\ 45°$ success in angular position of the radiation source. The proposed detector system functions both as a gamma counter and gamma source direction detector that is capable of measuring in a wide energy range. It is a portable, compact and light weighted device designed for mainly field applications and to be used by surveyors. The system provides remote data access to be used in high activity environment. It has a high accuracy in detection and angular position measurement results. The system also has high performance with a single chip operation that both filters, counts and calculates eight gamma counters concurrently. The device is suitable to be used with robotic systems or unmanned vehicles with its light weight and low power consumption.

2. MATERIAL AND METHOD

The main parts of detector system are detector probe, electronic boards, HMI unit, and metal chassis.

2.1 Detector Probe

The detector probe consists of a lead housing and PIN diode arrays. Among radiation sensors to be used in dosimetry applications, PIN diodes are more preferable with its advantages of high sensitivity, small size, good linearity, high quantum efficiency, quick response time and possibility to use with or without bias voltage depending on photovoltaic mode or photoconductive mode for different applications [27]. High photo and radiant sensitive BPW34 model silicon PIN type photodiodes have been chosen as a detector sensor. Its dimensions are 5.4 mm length, 5.4mm, 4.3 mm width, 3.2 mm height and 7.5 mm^2 radiant sensitive area. They are low-cost component with respect to the other radiation sensitive semiconductor components [28]. Four BPW34 diodes are connected parallel to increase the detector systems sensitive surface as 7.5 mm^2 ×4 that provides better detection performance [29]. The light sensitive PIN diodes are optically isolated by heath shrinks for filtering light noise but it causes the disadvantage of preventing alpha ray detection.

Although the active area of the photodiode is constant the width of the depletion layer can be modified by changing the applied reverse bias voltage. The photovoltaic mode provides minimum leakage current but has lower sensitivity due to the lower depletion layer. The photoconductive mode has higher sensitivity due to the increment of depletion layer proportional to the applied bias voltage but this increases the value of leakage current that limits the minimum measurable dose rate level. Also, a wider depletion region reduces the junction capacitance of photodiode. For a basic RC low-pass filter, reducing capacitance increases the cut-off frequency that allows for wider bandwidth that maximize the detectors ability to respond to rapid illumination variations. For these advantages photovoltaic mode was preferred for this design.

However, the increasing temperature also increases the leakage current, the studies show that the PIN diodes are suitable to be used in ambient room temperature. As parallel connection increases the detector area, this also has the drawbacks like increasing the dark current from 2.1 pA to 8.4 pA and also increases the junction capacitance 79.9 pF to sum of four BPW 34 capacitance [30].

The Compton scattering, photoelectric absorption and pair production are main possible interaction mechanisms for radiation detectors that results partially or complete energy transfer of the gamma-ray photon to electron energy. For perceiving the gamma rays in a directional way, surrounding of the photodiode array must be shielded with high Z materials that is preferably lead.

For this purpose, a lead housing detector has been designed and its slots are located in 8 different directions 45° apart from each other where the BPW34 arrays have

been placed. The layout of the PIN diode arrays has been adjusted to detect the gamma ray sources up to three detectors at any angular position as seen in (Fig. 1).
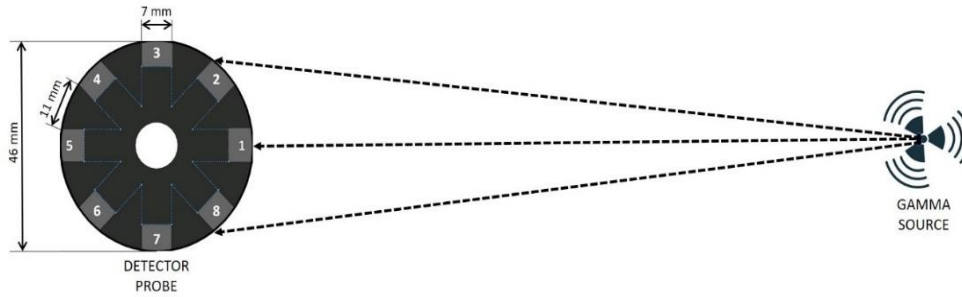
FIGURE 1. Detector PIN diode arrays layout and field of view for a gamma source.

The lead detector housing consists of two parts, the upper cover and the main body. There is a hole in the main body through which the cables from the sensors to the detector are placed. The lead housing has been produced by casting technique by using a 3D printed model as given in (Fig. 2a) for making moulds. The PIN diode arrays are placed in the housing an insulated from the main body and the upper cover of the housing by plastic film and epoxy resin. Each PIN diode array is embedded in the slots located on the lead housing having 11 mm thick separating walls that provides a directional view for the PIN diode arrays. The lead housing has also been covered with a 0.5 mm thick copper plate coated with 0.5 mm tin material to prevent the detection of secondary gamma and X-rays generated by the interactions of incoming gamma rays with the lead material (Fig. 2b). The BPW 34 arrays are placed in the slots of the lead housing as given in (Fig. 2c).

A flexible steel hose is placed between the probe and the unit that is used for holding and adjusting the inclination of the probe and used for shielding the detector cables form electromagnetic noise. For a shielding material with good geometry, the relation of transmitted photons number I and the number without an absorber material I_0 is given as:

$$\frac{I}{I_0} = e^{-\mu t} \tag{1}$$

where μ is the attenuation coefficient and t is the absorber materials thickness. For a bad geometry situation, the equation is modified as:

FIGURE 2. 3D printed mould model (a); shielded and insulated lead housing (b); assembly of BPW 34 arrays (c).

$$\frac{I}{I_0} = B(t, E_\gamma).e^{-\mu t} \tag{2}$$

where $B(t, E_\gamma)$ is the build-up factor that provides a multiplication correction. The calculated attenuation for the shielding including the build-up factor for ^{137}Cs is almost 70%. The results of the measurements of the angular response of the BPW-34 photodiode detector show that PIN diodes angular response normalized to 0° varies almost less than about 20% for radiation incidence angles ≤30° [31]. In consideration of these measurements and calculated attenuation, the shielded housing can be evaluated to provide a directional view for the sensors.

2.2 Electronic Boards

The electronic boards consist of the LNA detector boards for 8 channels, power system (high voltage board, battery, digital voltage display and detector voltage adjusting knob), the signal inverter board and the FPGA board units.

2.2.1 LNA Detector Boards

The LNA detector board is an improved version of the circuit used in a thesis [32]. The LNA board has four stages and the rest of the system is given in (Fig. 3).
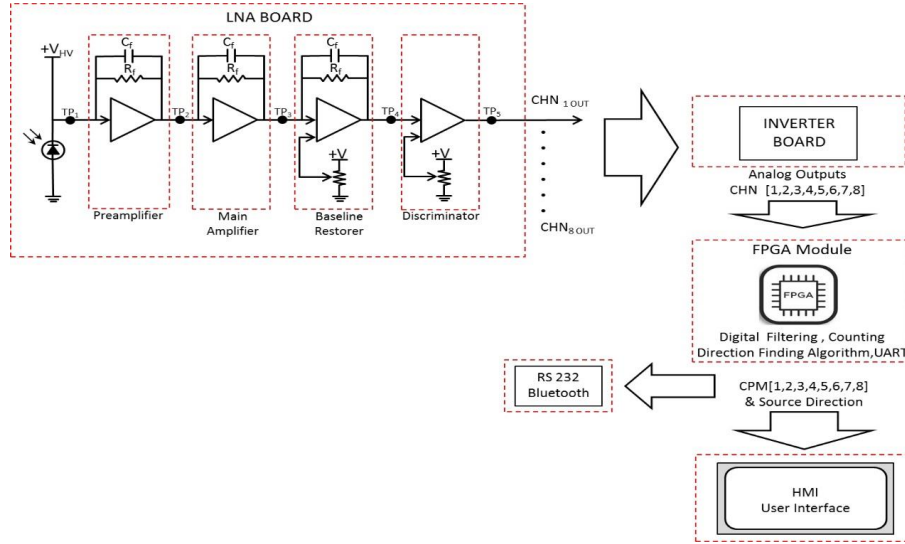
FIGURE 3. Numerical solution of the state-space model.

The preamplifier section of the LNA board operates as a charge to voltage converter and amplifies the charge of sensors into voltage pulses in millivolt levels. In this charge to voltage conversion, it is desired to preserve the waveform of the pulses [33]. In CSA (charge-sensitive amplifiers) the output voltage (V_{out}) is proportional to input charge and its input current (I_{in}) dependency is given by:

$$V_{out} \sim q_{in} = \int I_{in}(t).dt \tag{3}$$

A feedback capacitor C_f and a parallel connected feedback resistor forms a feedback impedance Z_f. The gain (g_{signal}) of the CSA is given by:

$$g_{signal} = \frac{V_{out}}{I_{in}} = -Z_{in} = -X_{C_f}//R_f = -\cfrac{1}{\cfrac{1}{R_f} + jwC_f} \tag{4}$$

and the decay time constant (τ_{decay}) is given by:

$$\tau_{decay} = R_f C_f \tag{5}$$

So, this gives a short time to obtain a correct charge-proportional voltage. As the detector output rises and falls in a short time, the rise time of the amplifier should be very quick and it should have low inner noise and linear response.

B. ÇUHADAROĞLU, H.G. İLK

The detector charge output will decrease exponentially in approximately 50 ns. The response of the preamplifier is tested by applying pulses generated by a square wave generator that has rise time less than 10 ns and the rise time of the LNA is measured as 40 ns. Different pulses with increasing voltages applied to test point over the capacitance 1 pF and the amplifiers output have been measured and their logarithmic graph is given in (Fig. 4).
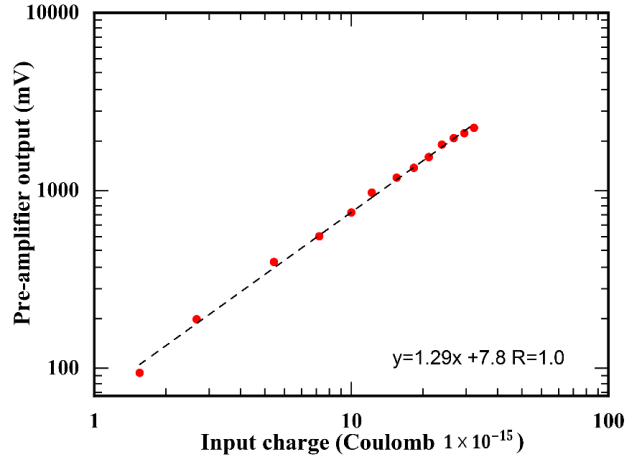
FIGURE 4. Numerical solution of the state-space model.

The second section is the main amplifier part of the LNA board. In addition to amplifying the pulses it also realizes the derivation and integration functions and changes the waveform of the output. By this operations sensor signals are cleared from noise and the fall time is decreased. The logarithmic graph of main amplifiers output voltage o versus the charge applied to the input is given in the (Fig. 5).

The third section is the baseline restorer part of the LNA board and used to lower the DC content of the signal to the ground level. This block also transmits and amplifies the signals to the output of the stage that are above the reference voltage which is adjusted by the potentiometer P_1. The fourth stage is the discriminator section where the discrimination level is adjusted by the potentiometer P_2 and the pulses above this level is transmitted to the output where the lower signals are rejected. The signals are measured by a HAMEG 2524 model 250 MHz digital oscilloscope and a screenshot of the LNA's preamplifier, main amplifier, baseline restorer, discriminator stages output waveforms are given in (Fig. 6), respectively.
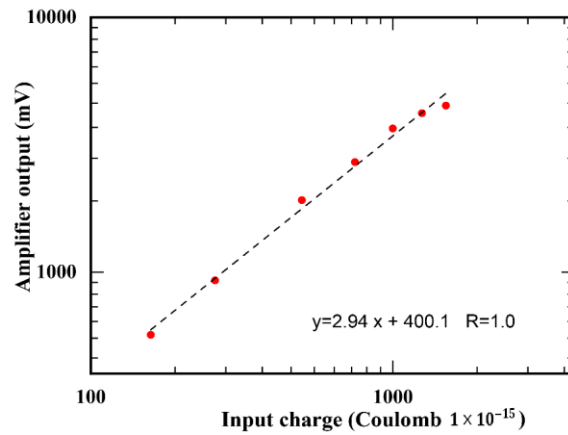
FIGURE 5. Amplifier stage charge to voltage conversion.
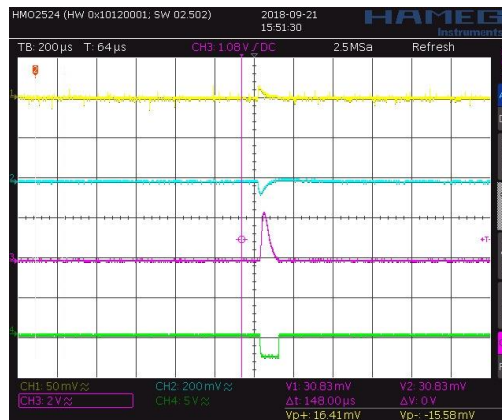
FIGURE 6. Output waveforms of the LNA's preamplifier, main amplifier, baseline restorer, discriminator Stages for a gamma interaction

The LNA is tested by increasing the frequency of square wave signals and results show that it can count up to 78 K pulses. When the PIN diode is exposed to a gamma source, the pulse width of the discriminator is measured from the scope and its value is found almost 30 microseconds. If this value is assumed to be the dead time of the counter, it can be assumed that the counter can count up to 35.000 counts/sec for this sensor type. The P1 is set to the position for the best measurement and the noise level of the discriminator input from the scope is measured almost ±46 mV. The P2

potentiometer value is also set accordingly to prevent the triggering of the discriminator by false measurements. Every LNA board is calibrated by using ^{137}Cs gamma source. Their baseline restorer and discriminator levels are calibrated by P_1 and P_2 potentiometers respectively. The power consumption of each LNA board is measured as 12.8 mA.

2.2.2. Detector Power System

12 V DC battery that provides portability and noise free operation. The maximum current value for the system has been measured as 247 mA with 12 V battery. The battery is also used for powering system and a DC-DC step-up high voltage board is used to invert 12V to up to 80 V to be applied detector feeding terminals of the LNA board. Feeding voltages at different voltage levels have been applied and an optimum level of 80 Volts has been chosen. 60V of the feeding voltage has been spent on the resistance and only 20 Volt of the input voltage has been applied over the PIN diode. The detector voltage is adjusted by the voltage knob and its voltage level is measured and displayed on the seven-segment display located in the front side of the detector. This provides an option to use various PIN diode detectors with different bias voltage levels and observe its effect on the detector efficiency and measurement noise.

However, the detector efficiency increases proportionally to the voltage increment, it also increases the noise and causes false detections. The measured noise level in the input of discriminator port in a radiation free environment have almost been almost $\pm$ 38 mV. The calibrations are done by setting the optimum operating points where the measurements are maximum and there is no pulse signal output when the gamma source is removed. Discriminator voltage is set to 46mV for filtering noise. Output signals of a single detector and LNA for a ^{137}Cs test source is given in (Fig. 7).

2.2.3 Signal Inverter Board

For this detector design, FPGA with IO's operating only in positive 0V-3.3 V voltage range has been chosen. The analog output pulse of LNA is negative and they have to be inverted into positive pulses and limited in the FPGA input range for counting. An inverter board with 8 channels is also designed to invert the negative pulses to positive scaling to the FPGAs 3.3 V level.
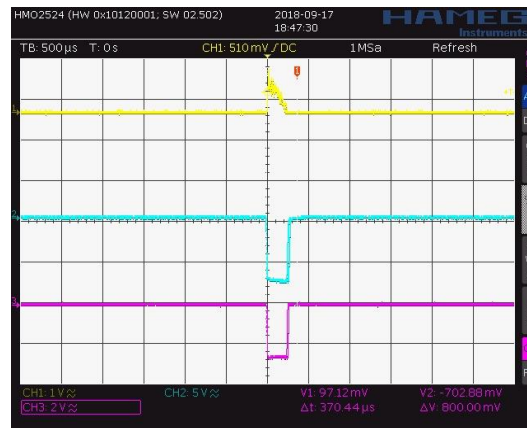
2.2.4 FPGA Unit

FIGURE 7. Numerical solution of the state-space model.

The system is based on the concurrent measurement of 8 gamma count based radiation detectors. In high activity environment, the detector output pulses increase and also the due to the narrow pulse width, the counter part of the detectors must be capable of operating with high frequency and high precision. The system requires 8 processors for each channel and a master processor for evaluating the measurements and calculating the angle. For meeting these requirements of the system, a XILINX Spartan 3E FPGA chip that is capable of parallel processing has been used. An individual module for each channel and other functions has been created by the gates and FPGA provides a single chip operation. The system code is written in VHDL language. The system has 8 independent, parallelly operating, concurrently running counter blocks embedded in the FPGA and results are calculated and refreshed in every minute. The FPGA has a 50 MHz clock frequency and the sampling period is set to 2μs. A signal conditioner block has written in VHDL to be used in every channel including filtering, metastability, debouncing, oversampling preventing and rising edge detection blocks for detecting signals with valid durations. However, the system can measure and display counts per second (cps). The measurements are usually fluctuating due to non-uniform exposure of radiation source. For providing a stable and more reliable angular values, counts are converted in counts per minute (cpm). The first cpm value can be displayed after a period of one minute. In order to give an early value before one minute is up, the measurements of each second beginning from the first second to the fifty-ninth second are multiplied by an appropriate coefficient and normalized to the one-minute value. By this option, the system starts displaying cpm since the power is on. The cpm value is calculated by the moving window technique and storing cps values FIFO data buffer. The counted cps values are updated every second.

In every second, the cpm values of 8 channels is updated and displayed and channels are given as CH_k and counts are given as cpm_k, where k is the channel indice and $k=$ [1,2,3,...,8], respectively. The first array is placed in 45° and the rest are placed 45° apart from each other. The direction of each array can be calculated by multiplying its array indice value with 45°. In each minute, the cpm values are updated and the cpm results array are evaluated. Among these measurements array, the indice of the maximum value is determined. The Direction of Source (*DOS*) can be calculated by multiplying the indice value "k" of the channel where maximum measurement is detected with 45° as given with equation:

$$DOS = k \times 45° \tag{6}$$

For example, if maximum count is received from the channel CH_3 then the result can be calculated by multiplying indice value k=3 with 45°, as *DOS*$= 3 \times 45° = 135°$. However, this approach provides a 45° resolution, the angular resolution cab be improved by applying some computational algorithms over the cpm measurements.

2.3 HMI Unit

A 5" NEXTION HMI is used for displaying the cpm and the detected source direction values that are serially transmitted to HMI from FPGA unit. Its user interface is designed and coded to display the counts received from the sensors, maximum count value, calculated angle of radiation incidence of source rays in accordance with the sensors zero angle point, a 360° scale that displays the direction of the source and buttons to navigate between the pages that display results in either cpm or cps units.

2.4 Metal Chassis

As the measurement is so sensitive and the detector signals levels are very low, the system is placed in an aluminum bag with dimensions 32×23×15.5 cm dimensions. The metal chassis is chosen for shielding electromagnetic noise and grounding. Metal mounting plates are also designed and manufactured for assembling the electronic hardware in the bag and isolating the electromagnetic noise interference between power, processor and LNA sections of the device. The whole detector assembly and its inside view is given in (Fig. 8a) and (Fig. 8b), respectively. The removable metal separator cover placed on the analog part helps to prevent the electromagnetic interference between the analog and digital blocks. In addition, calibration can be performed by reaching the trim pots of the baseline restorer and comparator parts of the LNA cards through the slit window on this cover part.

Additional mounting plates are placed inside the metal case to install the electronics. LNA cards are placed on the upper part of this system so that they can be easily removed and installed by their mounting parts. In the lower part, battery and high voltage cards are mounted. The total weight of the portable unit is measured as 3185 grams. The electronic system and metal assembly is given in (Fig. 9).

FIGURE 8. Detector unit assembly (a); Interior view of the detector (b).

FIGURE 9. The electronic system and metal assembly.

3. Results And Discussion

3.1 **The Calibration**

The calculations are based on comparison of cpm values from sensors having efficiencies identical to each other. For providing this condition firstly the backgrounds of the sensors are measured in a radiation source free environment and then the sensors are exposed to the same ^{137}Cs source from 2 cm distance and their cpm measurements are recorded for 15 minutes. The average counts of the sensors are calculated taking into account the background noise and each channels background count are subtracted from cpm values. The counts of every channel are recorded and their average cpm values (cpm_{avg}) are calculated. The ratios of each sensor over this average value are calculated and an array of calibration coefficients (*coef*) are calculated as given below:

$$cpm_{avg} = \sum_{1}^{k} cmp_k \qquad , k = [1, 2, 3, ..., 8] \qquad (7)$$

$$coef_k = \frac{cmp_k}{cpm_{avg}} \qquad (8)$$

The coefficients are multiplied by the actual cpm measurements (cpm_{act}) and corrected cpm values (cpm_{cor}) are evaluated for each sensor. The direction calculation algorithm is applied over these corrected count values and the source position direction is determined by the detector system.

3.2 **Detector Tests**

The efficiency of the detector was tested with the gamma sources. The experiments were performed in Institute of Nuclear Sciences, Ankara University. For measurements, a hand-made measuring mechanism consisting of a source holder apparatus that radiation source was attached and a rail with a length scale on it, which allowed the source to be positioned at the desired distance by sliding freely on it, was used as given in (Fig. 10).

Two types of test were performed; cpm vs distance measurements for different radioactive sources and source position angular measurements.

FIGURE 10. Source holder and sliding rail.

3.2.1 Cpm vs Distance Measurements For Various Radioactive Sources

The measurement sensitivity of the detector for radioactive sources (^{241}Am, ^{137}Cs, ^{60}Co) with various energy is tested by applying exposure to the detector. The used sources are given in (Fig. 11).

FIGURE 11. Radioactive sources (^{241}Am, ^{137}Cs, ^{60}Co).

Low activity laboratory point sources were used for radiation safety. The activity values and gamma ray energies of the used gamma ray test sources are listed in the Table 1.

TABLE 1. The activity and gamma ray energy of the gamma ray test sources.

Source Type	^{241}Am	^{137}Cs	^{60}Co
Activity	9.761 µCi	3.7 MBq	1 µCi
Energy	59.54 (keV)	661 (keV)	1173 (keV) and 1332 (keV)

^{60}Co source having highest gamma ray energy and ^{241}Am source having lowest gamma ray energy were chosen for determining the detectors energy measurement range.

Each test sources were positioned in front of the detector and counted one by one. Each measurement was taken for 5 minutes and their average cpm measurements was recorded. cpm measurements versus distance was taken by moving the gamma radiation sources position in 1 cm steps. The measurement range mainly depended on the activity of the gamma ray source. It was observed that the cpm values taken according to increasing distance measurements decreased inversely proportional to the square of the source distance in accordance to inverse square law [34] as given:

$$\Phi \propto \geq \frac{1}{r^2} \tag{9}$$

where Φ is the radiation flux and r is the distance value between the radiation test source and the point where radiation flux is to be calculated.

The cpm values versus distance of the [241]Am, ^{137}Cs, ^{60}Co sources are given in (Fig. 12), (Fig. 13) and (Fig. 14), respectively.
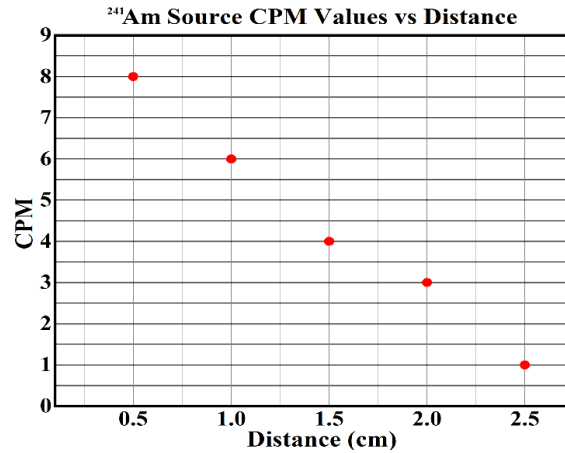
FIGURE 12. [241]Am source cpm values vs distance.
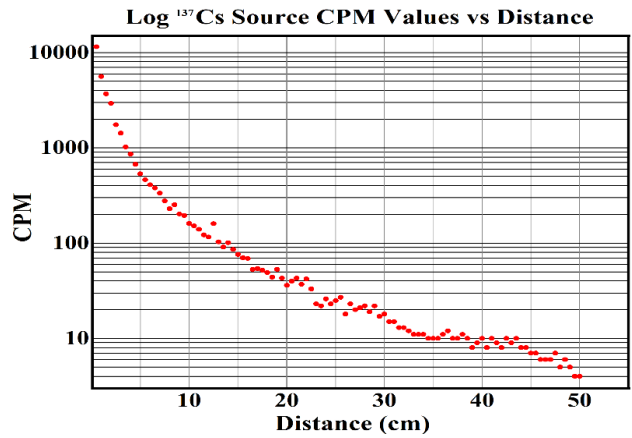
FIGURE 13. Logarithmic ^{137}Cs source cpm values vs distance.
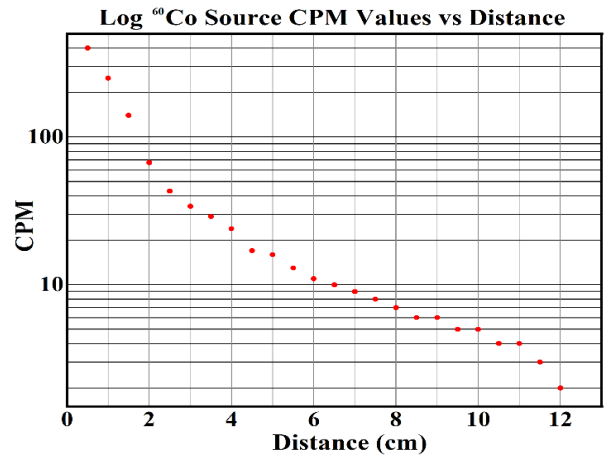
FIGURE 14. Logarithmic ^{60}Co source cpm values vs distance.

The test results show that the system can detect gamma rays within the range starting from 59.54 keV to 1332 keV and it operates as a gamma detector and gamma counter unit. The cpm values decrease inversely proportional to the square of the gamma ray test source position distance due to the inverse square law and the detector distance range can be increased by using sources with higher activity.

3.2.2 **Source Position Angle Measurements**

In the next step, the detector probe was placed in the center of a 360° protractor scale for performing the angular measurements of the equipment. The measurements were taken by increasing angle from 0° to 360° with 10° steps. For every angle steps the cpm and radiation source angle values were measured by moving the radiation source located in the holder mechanism away from the center of the probe in 1 cm steps for the distance values 0 cm to 50 cm. For every angle position the sliding radiation source holder aligned and positioned to the measurement angle with respect to the angle scale on the protractor. The system measures all eight channels concurrently and detects the channel with the highest cpm values. After this the incidence angle were calculated by using the indice of the channel with maximum count and the result were numerically displayed and also shown on the digital scale of the user interface. The measurement results were plotted in a 360° scale vs distance as shown in (Fig. 15). As can be seen from the results in the graph (Fig. 15), it can be said that the detector has successfully detected the angle where the ^{137}Cs radiation source is placed for the test. Although the angle detection performance of the system was within acceptable limits, some deviations were detected in some measurements. In order to examine the performance of the tested system in detail, the angular measurements were drawn versus distance for ±10° measurement intervals in 360° scale. The most of the results are within ±45° interval. 14 of 1800 angle measurement is out of this interval and its success is 99.22 %.

i. The false measurements are shown with red legends. These measurements are concentrated at positions closer to the center. The source has a high activity and the gamma flux is increasing when the source is closer to the sensors. The gamma source is located on the tip of an aluminum cylinder located in the center of the disc and it was hard to handle and manage its orientation to the required angle. The source was aligned in each step but even the smallest angular deviations made during the placement of the point source cause a larger angular difference in calculations due to higher flux at close positions. This may be the reason for the false measurements.

ii. According to the graph it is seen that some of the angular measurement values of 20°, 110°, 160°, 250°, 290°, 340° were deviated from source angular positions. However, the detectors have directional view, incorrect measurements may occur due to the high cpm values at close range at angles 67.5°, 112.5°, 157.5°, 202.5°, 247.5°, 292.5°and 337.5°, which are the intersection values of the viewing angles of neighboring detectors. This may be the reason for false measurements that are taken for the angular positions close to these intersection angles and source positions close to the detector center.
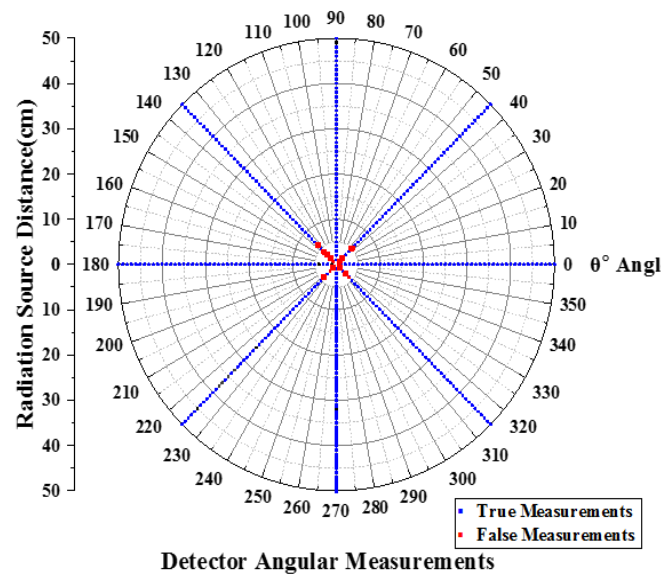
FIGURE 15. Distance vs angular measurements.

iii.   The solid angle seen by the sensor decreases and becomes sharper as the source gets further away. As a result of this, it is observed that the detector's angle estimation performance increases as the source moves further.

iv.   After detecting the direction within 45°, a more precise angle value be determined by rotating the detector till it is aligned with the source position angle and reaches the maximum cpm count. Angular detection performance can be improved by applying this technique.

4. CONCLUSIONS

In this study, an ionizing radiation detector system that can both detect the ionizing gamma source and estimate direction of the radiation source numerically and also can display the direction angle on a scale has been designed, its prototype was manufactured and tested with radioactive sources. It has been observed that the device is capable of measuring in a wide range of gamma sources like ^{241}Am that has the lowest energy, to ^{60}Co that has highest energy. The system also operates as a gamma counter device and takes cpm measurements concurrently with 8 individual channels. The device has also been tested with a ^{137}Cs source for positions at angles ranging from 0° to 360° and for different distances ranging from 0 cm to 50 cm and

36×50 measurements were taken. The results have showed that the device can accurately determine the direction where the radiation source is located. Although the device has initially been manufactured a little bigger for a prototype design purpose, it is still a light, portable and compact hand-held detector unit. It is possible to manufacture the detector with less than half of the existing dimensions by using surface mounted circuit elements and multi-level cards if desired. With its low power consumption, portable design and light weight, this system can be used in the field as a handheld detector by surveyors, can be mounted on air and over land vehicles. It is also suitable to be mounted on radiation survey robots and provide angular data to reach the source directly. The system can be used at security crossing points for safety purposes. By the serial data port and Bluetooth on it, the system enables remote data reading in high-activity risk areas where researchers cannot approach or cannot stay for a long time due to high radiation exposure.

The suggested detector unit is a multisensor system that can count incident rays over each sensor concurrently. The angular resolution can be improved by applying computational algorithms over the evaluated cpm results. Both of the range and efficiency of the detector system can also be improved by using scintillator crystal coupled PIN diodes with larger detection surface. The weight and the dimensions of the system can be reduced by using SMD components multilayer boards to be used in UAVs, robotic system or to be used in field by surveyors. However, this system is based on a Geiger-Müller gamma counting method, the system can also be used as an isotope identifier after adding a proper analog to digital converter (ADC) to the output of the low noise amplifier block.

REFERENCES

[1] IAEA-TECDOC-804 Methods to identify and locate spent radiation sources. (2021, May 24). https://www-pub.iaea.org/MTCD/Publications/PDF/te_804_prn.pdf

[2] Kroeger, R.A. et al., Spatial resolution and imaging of gamma rays with germanium strip detectors, SPIE, 2518 (1995), 236. https://doi.org/10.1117/12.218379

[3] Kroeger, R.A., Gehrels, N., Johnson, W.N., Kurfess, J.D., Phlips, B.P., Tueller, J., Charge spreading and position sensitivity in a segmented planar germanium detector, *Nucl. Instrum. Methods Phys. Res. A*, 422 (1999), 206-210. https://doi.org/10.1016/S0168-9002(98)01095-X

[4] Kroeger, R.A., Johnson, W.N., Kurfess, J.D., Phlips, B.F., Gamma ray polarimetry using a position sensitive germanium detector, *Nucl. Instrum. Methods Phys. Res. A*, 436 (1999), 165-169. https://doi.org/10.1016/S0168-9002(99)00615-4

[5] Kurfess, J.D., Johnson, W.N., Kroeger, R.A., Phlips, B.F., Wulf, E.A., Development and applications of position-sensitive solid-state gamma ray detectors, *Nucl. Instrum. Methods Phys. Res. A*, 505 (2003), 256–264. https://doi.org/10.1016/S0168-9002(03)01064-7

[6] Vetter, K., Burks, M., Mihailescu, L., Gamma-ray imaging with position-sensitive HPGe detectors, *Nucl. Instrum. Methods Phys. Res. A*, 525 (2004), 322–327. https://doi.org/10.1016/j.nima.2004.03.087

[7] Gerl, J., Korten, W., AGATA technical proposal, GSI Report, Darmstadt, 2001.

[8] Deleplanque, M.A., et al., GRETA: utilizing new concepts in γ-ray detection, *Nucl. Instrum. Methods Phys. Res. A*, 430 (1999), 292-310. https://doi.org/10.1016/S0168-9002(99)00187-4

[9] Milechina, L., Cederwall, B., Performance considerations for g-ray tracking detectors, *Nucl. Instrum. Methods Phys. Res. A*, 525 (2004), 208-212. https://doi.org/10.1016/j.nima.2004.03.047

[10] Fujimoto, K., Noda, Y., Gamma ray direction finder, *Radioact. Environ.*, 7 (2005) 118-125. https://doi.org/10.1016/S1569-4860(04)07012-3

[11] Fujimoto, K., A simple gamma ray direction finder, *Health Phys.*, 91 (2006), 29-35. https://doi.org/10.1097/01.HP.0000196113.49929.be

[12] Tajima, H., et al., Design and performance of the soft gamma-ray detector for the NeXT mission, *IEEE Trans. Nuc. Sci.*, 52 (6) (2005), 2749-2757. https://doi.org/10.1109/TNS.2005.862776

[13] Shirakawa, Y., Development of a direction-finding gamma-ray detector, *Nucl. Instrum. Methods Phys. Res. B*, 263 (2007), 58-62. https://doi.org/10.1016/j.nimb.2007.04.056

[14] Shirakawa, Y., Yamano, T., Kobayashi, Y., Remote sensing of nuclear accidents using a direction finding detector, 35th Annual Conference of IEEE Industrial Electronics, 2009. https://doi.org/10.1109/IECON.2009.5414850

[15] Dung, T.Q., Thanh, N.D., Tuyen, L.A., Son, L.T., Phuc, P.T., Evaluation of a gamma technique for the assay of radioactive waste drums using two measurements from opposing directions, *App. Radiat. Isot.*, 67 (2009), 164-169. https://doi.org/10.1016/j.apradiso.2008.08.008

[16] Hindi, M.M., Klynn, L., Demroff, H., Gamma vector camera: A gamma ray and neutron directional detector, IEEE Conference on Technologies for Homeland Security, 2008. https://doi.org/10.1109/THS.2008.4534502

[17] Schemm, N., Balkır, S., Hoffman, M.W., Bauer, M., A directional gamma ray detector using a single chip computational sensor, IEEE Sensors, 2011. https://doi.org/10.1109/ICSENS.2011.6127024

[18] Wahl, C.G., He, Z., Gamma-ray point-source detection in unknown background using 3D-position-sensitive semiconductor detectors, *IEEE Trans. Nuc. Sci.*, 58 (3) (2011), 605-613. https://doi.org/ 10.1109/TNS.2011.2113355

[19] Akkoyun, S., A method for determination of gamma-ray direction in space, *Acta Astronautica*, 87 (2013) 147-152. https://doi.org/10.1016/j.actaastro.2013.02.012

[20] Becker, E.M., Farsoni, A.T., A multi-panel direction-sensitive gamma-ray detector for low-altitude radiological searches, *Nucl. Instrum. Methods Phys. Res. A*, 836 (2016), 13-21. https://doi.org/10.1016/j.nima.2016.08.011

[21] Bukartas, A., Finck, R., Wallin, J., Rääf, C.L., A Bayesian method to localize lost gamma sources, *App. Radiat. Isot.*, 145 (2019), 142–147. https://doi.org/10.1016/j.apradiso.2018.11.008

[22] Gabrlik, P., Lazna, T., Simulation of gamma radiation mapping using an unmanned aerial system, *IFAC Papers OnLine*, 51 (6) (2018), 256-262. https://doi.org/10.1016/j.ifacol.2018.07.163

[23] FitzGerald, J.G.M., A rotating scatter mask for inexpensive gamma-ray imaging in orphan source search: Simulation results, *IEEE Trans. Nucl. Sci.*, 62 (1) (2015), 340-348. https://doi.org/10.1109/TNS.2014.2379332

[24] Holland, D.E., Bevins, J.E., Burggraf, L.W., O'Day, B.E., Rotating scatter mask optimization for gamma source direction identification, *Nucl. Instrum. Methods Phys. Res. A*, 901 (2018), 104-111. https://doi.org/10.1016/j.nima.2018.05.037

[25] Olesen, R.J., O'Day, B.E., Holland, D.E., Burggraf, L.W., Bevins, J.E., Characterization of novel rotating scatter mask designs for gamma direction identification, *Nucl. Instrum. Methods Phys. Res. A*, 954 (2020), 161232. https://doi.org/10.1016/j.nima.2018.09.067

[26] Karafasoulis, K., Zachariadou, K., Seferlis, S., Kaissas, I., Lambropoulos, C., Loukas, D., Potiriadis, C., Simulated performance of algorithms for the localization of radioactive sources from a position sensitive radiation detecting system (COCAE), 11th International Conference on Applications of Nuclear Techniques, (2011). https://doi.org/10.1063/1.3665338

[27] Bueno, C.C., Gonçalves, J.A.C., de Magalhães, R.R., Santos, M.D.S., Response of PIN diodes as room temperature photon detectors, *App. Radiat. Isot.*, 61 (2004), 1343-1347. https://doi.org/10.1016/j.apradiso.2004.03.064

[28] Silicon PIN Photodiode BPW34, BPW34S. (2021, Feburary 23) https://www.vishay.com/docs/81521/bpw34.pdf

[29] Andjelkovi, M.S., et al., Feasibility study of a current mode gamma radiation dosimeter based on a commercial PIN photodiode and a custom-made auto-ranging electrometer, *Nucl. Technol. Radiat. Prot.*, 28 (1) (2013), 73-83. https://doi.org/10.2298/NTRP1301073A

[30] Glenn, F., Knoll-Radiation Detection and Measurement, 4th ed., John Wiley&Sons, USA, 2010.

[31] Alvarez, J.T., Khoury, H.J., Hazin, C.A., Austerlitz, C., Angular response of a commercial photodiode in secondary standard fields of 90Sr/90Y beta radiation, *Radiat. Prot. Dosim.*, 66 (1) (1996), 451-453. https://doi.org/10.1093/oxfordjournals.rpd.a031776

[32] Özgen, S., Bir radyasyon sayacı geliştirilmesi ve çeşitli ortamlarda radyasyon ölçümü. M.S. Thesis, Fırat University, (2021). https://tez.yok.gov.tr/UlusalTezMerkezi/tezDetay.jsp?id =89Unyfp_2iJ5Ppy5Yz3Z1A&no=89Unyfp_2iJ5Ppy5Yz3Z1A

[33] Iniewski, K., Electronics for Radiation Detection, CRC Press, Boca Raton, 2011.

[34] Ahmed, S.N., Physics and Engineering of Radiation Detection, Academic Press, San Diego, 2007.

GEANT4 BASED DOSIMETRY EVALUATION FOR GAMMA KNIFE USING DIFFERENT PHANTOM MATERIALS

Özlem DAGLI[1], Erkan BOSTANCI[2], Ömer Hakan EMMEZ[1], Gökhan KURT[1], Fatih EKİNCİ[3] and Mehmet Serdar GÜZEL[2]

[1]Department of Neurosurgery, Gazi University, Ankara, TURKEY
[2]Computer Engineering Department, Ankara University, Ankara, TURKEY
[3]Physics Department, Gazi University, Ankara, TURKEY

ABSTRACT. This study examines the dose difference for a variety of phantom materials that can be employed for "Leksell Gamma" Knifes. These materials resemble human tissue by not including the skull bone. Geant4 was utilized in the analysis of the dose distributions for collimator helmet sizes of 4mm and 8mm. The phantom is illustrated with a radius of 80mm. Water, brain, Poly-methyl methacrylate (PMMA) and polystyrene were being considered as the main material types. Results proved that there is no considerable differences for radiation dosimetries depending on the material types. In addition, the polystyrene and PMMA (phantom is also quite appropriate in terms of evaluating the dose profiles of the Gamma Knife unit.

1. INTRODUCTION

Gamma Knife device developed in 1950s, was first presented in 1967 using 179 Co-60 sources. Early Acoustic Neuroma patient, was treated by Leksell in1969. In 1975 the second gamma knife device was established under the Karolinska Institute and Brain Surgery service. The third and fourth units were used in Buenos Aires, Argentina and Sheffield, UK. It was initially applied to functional neurosurgery patients and then to some benign tumors and small sized malignant tumors in the 1980s. The primary 201 Cobalt-60 sources Gamma Knife was founded in the USA in 1987 and later sophisticated the Model C followed by 192 Cobalt-60 sources Leksell Gamma Knife Perfexion. Gamma Knife Icon is the sixth and recent generation of the Leksell Gamma Knife technology [1].

Radiosurgery, a conformational treatment method, involves directing target bunches of beams from a number of different angles, resulting in rapid dose droping in normal tissues outside the target, while high doses are achieved in the confluence of the rays.

Leksell Gamma Knife radiosurgery comprises no institutionary surgical cuts for brain surgery operations [2]. The principle of Gamma Knife radiosurgery is incomplex. GammaPlan studies a tissue equivalent material, with a coefficient of attenuation, namely, "μ =0.0063 mm-1 at the energy 1.25 MeV", in all calculations deprived of the existing of a skull bone. Furthermore, in repetitive quality assurance programs of the Gamma Knife unit, a spherical polystyrene phantom is studied to provide dose distributions with the opening of all 201 "^{60}Co" sources. This phantom might not be completely tissue equivalent. Consequently, compatibility of these dose distributions is complicated [3]. In the proposed study, Geant4 is employed to compute the radial dose distributions obtained from a single radiation beam of 4 mm and 8 mm collimator helmet in variant phantom materials.

The source of radiation received in radiotherapy can be particle-based as well as gamma [4,5]. Different sources of radiation cause different reactions within the target [6]. Simultaneously, the increasing importance of radiation-related applications in our lives has increased the importance of measuring the amount of radiation received by living organisms or any material exposed to radiation [7].

Geant 4 is a Monte Carlo simulation software with a large library of physics, including tools that can simulate absolutely the interaction of the particles with the target. Geant name, "it was created using the geometry and Tracking words. While the major goal of the software growth is high energy physics experiment simulations, it is so used in many areas such as nuclear physics, medical and astrophysics today owing to the success and requirements of detector simulations. Also, the The Turkish Accelerator and Radiation Laboratory in Ankara, abbreviated as the TARLA facility, is proposed as the first facility of Turkish Accelerator Center (TAC) project where such detector simulations are made in Turkey. The main target of the TARLA facility is to build up a user facility to open up recent opportunities for interdisciplinary scientific research and applications, as materials science, medicine, nanotechnology, life sciences, etc [8,9].

There are several ways to get a Geant4 simulation for a particular problem. The easiest is to use a ready-made application or tool that provides the essential qualifications to create an installation or detector adapted to the field of application and to measure the observables. At the basis of Geant4 software, a category scheme is needed for the designed detector structure to be able to determine both geometric

and physical phenomena and read the results. Starting from the root of the scheme and moving upwards, the essential structures and procedures for the simulation are performed, so that a subaltern structure of the simulation operation in a certain order and order is created [10].

In this study, dosimetry calculations were made for different phantom materials that can be employed for Leksell Gamma Knife device. Water, brain, PMMA and polystyrene were used as the phantom material types. Solid water, brain, PMMA and polystyrene phantom taken into consideration and the design of the skull and device source was made with the Geant-4 computer-based program, and the target doses were determined.

The rest of the paper is structured as follows: Section 2 describes the material and the method employed in our study, followed by Section 3 where findings are presented and discussed. Finally, the paper is concluded in Section 4.

2. MATERIAL AND METHOD

In the study, a Gamma Knife device, brain phantom was simulated using Geant4. The Gamma Knife Device (GK) used was the 4C model with 201 sources. Phantoms are materials that are equivalent to human tissue and which are used to examine dose distributions in tissue. Studies with these phantom in the medical fields have been popular lately. For example, in dentistry, tissue-equivalent phantom was used to calculate dose rates of tumors at different depths with proton therapy.

This study mainly proposes to employ Geant4 platform, using Monte Carlo algorithms, to compute the radial dose distributions obtained from a single radiation beam of 8 mm and 14 mm collimator helmet in altered phantom materials. The material compositions of these phantom obtained from ICRP [11] are shown in Table 1.

TABLE 1. Phantom materials used in the analysis.

Component Name	Chemical Formula	Density
PMMA	$(C_5O_2H_8)_n$	1,18 g/ml
Polystyrene	$(C_8H_8)_n$	0.96–1.05 g/ml

In this study, a 80 mm radius phantom was used. As a phantom material are selected solid water, brain, PMMA (poly-methyl methacrylate) and polystyrene.

Geant4 is a modern Monte Carlo simulation program that emerged in 1993 with the work of scientists at CERN (European Organization for Nuclear Research), which can simulate particles interacting with matter. The name Geant is derived from the words "GEometry ANd Tracking" [12].

In Geant4 application, firstly, the preparation of geometry such as materials to be simulated, volumes and locations; description of related physics such as particles, physical processes, models and production threshold energy; formation mechanism of primary particles; display of prepared geometry and particle traces; adding user User Interface (UI) commands; During the simulation, necessary information must be collected [13].

For the simulation application of the Gamma Knife device, a new modular design was made by using the documentation of the existing system and taking its technical features. The aim here is to define the gamma beam profile and to reveal the most appropriate and useful structure for obtaining beam profile by using existing irradiation-collimator materials.

In the Geant4 simulation program, while preparing the simulation software of the Gamma Knife system, four basic steps were taken into consideration: 1) Defining the general structure, 2) creating the physical geometry, 3) defining the physics events and 4) simulation process and calculations.

3D models of Gamma Knife design were prepared and preliminary graphic models for simulation were created in computer environment. The 3D designs of the source are shown in Figure 1 below [14].

The shapes forming three basic geometric structures as World, Target and Tracker are defined with codes in Geant4 software. According to this definition, the world; A room with an indoor environment of 400x400 cm^2 air represents the position in the modeling and the model of the environment where the experiment will take place.

Target was defined as $90 \times 90 \times 90$ mm voxel detector plate. Other materials were also defined as similarly. These definitions; While creating the basic geometric structure, the collimator head and dimensions that ensure the exact fit of the model are defined. Geometric definitions of other objects are made similarly [16].

In the last step of the simulation study; It includes simulation processes and physical calculations in a way that is exactly appropriate for the model. The Gamma knife device consists of a hemispherical iron-coated unit containing 201 co-60 sources.
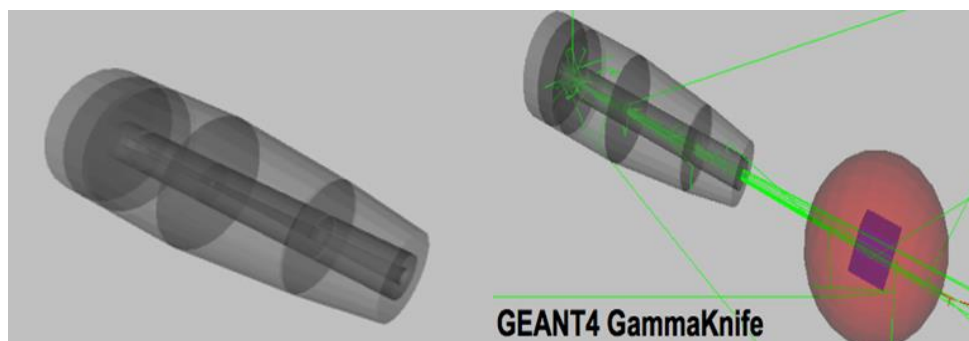
FIGURE 1. 3D resource design with Geant4 [15].

Gamma rays come from different directions and focus on the target.

Calculations were made for 4, 8 mm collimators. The stored energy was calculated at the end of the simulation in voxels divided into small 90x90x90 mm cubes using scoring mesh.

In the modeling study, firstly, instead of 201, the gamma ray originating from a single source was taken as a reference and calculations were made for 201 sources at different angles.

While modeling, the spherical water phantom having a radius of "80 mm", the brain phantom taken from ICRU data, PMMA (Poly-methyl methacrylate) and polystyrene phantom were used in dosimetric measurements (ICRU). The distance between patient source is 401 mm. Two gamma rays of 1.17 MeV and 1.33 MeV are released from the Co-60 decay. The stored energy was plotted by normalizing the dose with the data taken from the simulations.

3. RESULTS AND DISCUSSION

The simulation results were used to analyze the differences between varying embolization materials. The findings are described in the following.

The absorbed doses were compared in Table 2. The difference between the brain and the water phantom was observed as 12.5% and 7.9% for collimators with diameters of 4mm and 8 mm, respectively. The difference between the brain and the PMMA phantom was found as 12.6% when using a 4mm diameter collimator while it was 1.4% for the 8mm diameter collimator. The difference between the brain and the

Polystyrene phantom was observed as 6.2% and 3.6% for collimators with diameters of 4mm and 8 mm, respectively.

TABLE 2. Comparison of absorbed doses for different phantoms materials.

Collimator helmet size	Mean peak dose Phantom (a)	Mean peak dose Phantom (b)	% difference |(a-b)|×100/a
4 mm	Brain 0,8420	Water 0.9473	12.5
		PMMA 0.9481	12.6
		Polystyrene 0.8945	6.2
8 mm	Brain 0,9268	Water 0.8530	7.9
		PMMA 0.9399	1.4
		Polystyrene 0.8928	3.6

When Figures 2 and 3 are examined, it can be seen that the normalized dose curve expands as the collimator diameter increases. That is, as the collimator diameter increased, normal tissue received more doses. In addition, another observation is that as the collimator diameter increases, the margin of error decreases according to Table 2.
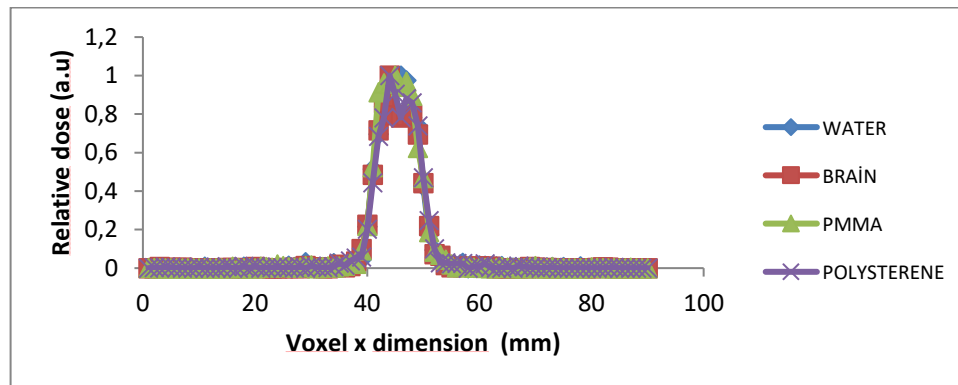
FIGURE 2. An evaluation graph of radial doses obtained from different phantom materials (4 mm collimator helmet of the "Leksell Gamma Knife").
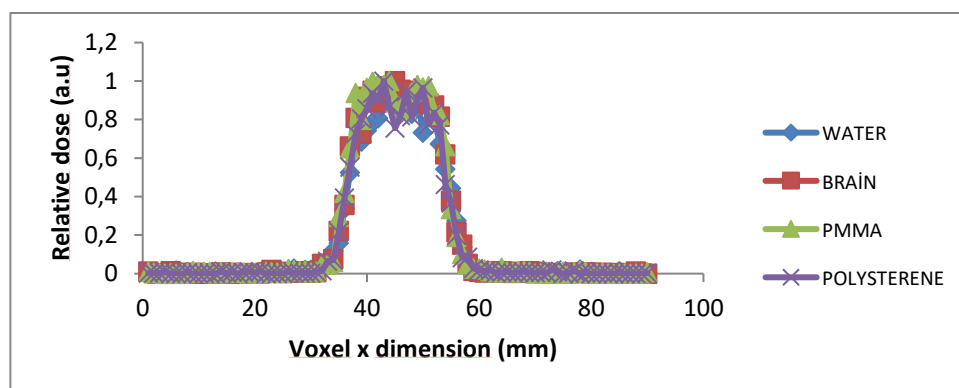
FIGURE 3. An evaluation graph of radial doses obtained from different phantom materials (8 mm collimator helmet of the "Leksell Gamma Knife").

Table 3 shows the results of the t-test performed to find out whether there are significant differences in the dose difference computed for different embolization materials. The simulations were run 10 times and the dose accumulations are compared. From the results, one can conclude that there are significant differences between water and brain while the differences of PMMA and Polystyrene were not found to be statistically significant.

TABLE 3. Statistical evaluation of dose differences of phantom materials with brain t-test.

	Water	PMMA	Polystyrene
"t Stat"	4.031180	-0.277680	1.120481
"P(T<=t) one-tailed"	0.000713	0.392812	0.141391
"t critical , one tailed"	1.770933	1.770933	1.770933
"P(T<=t) two-tailed"	0.001426	0.785624	0.282782
"t critical , two tailed"	2.160369	2.160369	2.160369

4. CONCLUSIONS

The correct determination of the radiation dose given to the patient is critically important. Therefore, phantoms are used that are equivalent to human tissue and examine the dose distribution in the tissue.

Our results show that the differences between the dose values using Geant4 for solid water phantom, brain, PMMA and polystyrene are remarkable. The percentage difference of Table 1 indicates some differences; however, these differences were not found to be statistically significant when the t-test was applied. Furthermore, these differences in statistical terms are not larger than the acceptable range ($< 3\%$) prescribed by the stereotactic radiosurgery. Results reveal different radiation dosimetries based on the material types. Besides, the polystyrene and PMMA phantoms are also appropriate for determining the dose profiles of the Gamma Knife unit as can be seen in [17].

Dose distribution in Leksell Gamma Plan (LGP) was calculated based on a homogeneous phantom. Different results can be obtained when materials of different densities are involved into the experimental process. Result encourage authors to adapt Geant4 simulations to investigate further problems regarding SRS [18].

Author Contribution Statements O.D. and E.B. designed the model and the computational framework and analysed the data. O.D. carried out the implementation and performed the calculations. O.D. and E.B. wrote the manuscript with input from all authors. H.E., G.K., F.E. and M.S.G. conceived the study and were in charge of overall direction and planning. In addition, all authors discussed the entire study and approved the final version.

Declaration of Competing Interests The authors declare that they have no known competing financial interests or personal relationships that could have appeared to influence the work reported in this paper.

REFERENCES

[1] Bertolino, N., Experimental validation of Monte Carlo simulation of Leksell Gamma Knife Perfexion stereotactic radiosurgery system. PhD Thesis, Università Degli Studi Di Milano, (2009), 6-17.

[2] Goetsch, S.J., Risk analysis of Leksell Gamma Knife Model C with automatic positioning system, *Int. J. Radiat. Oncol. Biol. Phys.*, 52 (2002), 869-877. https://doi.org/:10.1016/s0360-3016(01)02718-3

[3] Leksell Gamma Plan Instructions for Use for Version 4.0-Target Series, Elekta, 1996.

[4] Ekinci, F., Bostanci, E., Dagli, O., Guzel, M.S., Analysis of Bragg curve parameters and lateral straggle for proton and carbon beams, *Commun. Fac. Sci. Univ. Ank. Ser. A2-A3*, 63 (1) (2021), 32-41. https://doi.org/:10.33769/aupse.864475

[5]   Dagli, O., Bostanci, E., Emmez, O.H., Ekinci, F., Celtikci, E., A statistical analysis of the effect of different embolization materials on Gamma Knife arteriovenous malformation dose distributions, arXiv:2101.08034 (2021). https://arxiv.org/abs/2101.08034

[6]   Ekinci, F., Bostanci, E., Dagli, O., Guzel, M.S., Recoil analysis for heavy ion beams, arXiv:2101.09720 (2021). https://arxiv.org/abs/2101.09720

[7]   ICRU Report 62 Prescribing, Recording and Reporting Photo Beam Therapy (Supplement to ICRU Report 50), Bethesda, (1999).

[8]   Aksoy, A., Karsli, O., Aydin, A., Kaya, C., Ketenoglu, B., Ketenoglu, D. and Yavas, O. Current status of Turkish accelerator and radiation laboratory in Ankara: the TARLA facility, *Can. J. Phys.*, 96 (7) (2018), 837-842. https://doi.org/10.1139/cjp-2017-0750

[9]   Ketenoglu, D., Bostanci, E., Aydin, A., Ketenoglu, B., A hard X-ray self-amplified spontaneous emission free-electron laser optimization using evolutionary algorithms for dedicated user applications, *Turk. J. Phys.*, 43 (2019), 551-555. https://doi.org/10.3906/fiz-1909-5

[10] Agostinelli, S., Allision, J., Amaka, K., Apostolakis, J., Araujo, H., Arce, P., et al., GEANT4-A simulation toolkit, *Nucl. Instrum. Methods Phys. Res. A*, 506 (2003), 250-303. https://doi.org/10.1016/S0168-9002(03)01368-8

[11] ICPR. (2010, Feburary 10). https://physics.nist.gov/cgi-bin/Star/compos.pl?matno=123

[12] Li, J.S., Ma, C.M., A method to reduce the statistical uncertainty caused by high energy cutoffs in Monte Carlo treatment planning, *J. Phys. Conf. Ser.,* 102 (2008), 012015. https://doi.org/:10.1088/1742-6596/102/1/012015

[13] KEK, Geant4 Toolkit for the simulation. (2010, Feburary 10). http://www-geant4.kek.jp/

[14] Cuttone, G., Mongelli, V., Romano, F., Russo, G., Sabini, M., Geant4 based simulation of the Leksell Gamma Knife for treatment planning validations, 14th Geant4 Users and Collaboration Workshop, Catania, Italy, (2009).

[15] Dağlı, Ö., Tanır, A.G., Kurt, G., Analysis of radiation dose distribution Inhomogenity effects in Gamma Knife radiosurgery using Geant4, *Politeknik Dergisi,* (2021). https://doi.org/10.2339/politeknik.674718

[16] Sandilos, P., Tatsis, E., Vlachos, L., Dardoufas, C., Karaiskos, P., Georgiou, E., and Angelopoulos, A., Mechanical and dose delivery accuracy evaluation in radiosurgery using polymer gels, *J. Appl. Clin. Med. Phys*., 7 (4) (2006), 13-21. https://doi.org/:10.1120/jacmp.v7i4.2273

[17] Cheung, J.Y.C., Yu, K.N., Yu, C.P., Ho, R.T.K., Choice of phantom materials for dosimetry of Leksell Gamma Knife unit: A Monte Carlo study, *Med. Phys.,* 29 (10) (2002), 2260. https://doi.org/:10.1118/1.1508797

[18] Senirkentli, B.G., Ekinci, F., Bostanci, E., Guzel, M.S., Dagli, O., Karim, A., Mishra, A., Proton therapy for Mandibula plate phantom, *Healthcare*, 9 (2) (2021), 167. https://doi.org/:10.3390/healthcare9020167

ESTIMATING THE FREQUENCY AND BANDWIDTH OF SQUARE-SPLIT RING RESONATOR (S-SRR) DESIGNS VIA SUPPORT VECTOR MACHINES (SVM)

Sultan CAN[1] and Gökhan SOYSAL[1]

[1]Department of Electrical and Electronics Engineering, Engineering Faculty,
Ankara University, Ankara, TURKEY

ABSTRACT. In this study Support Vector Machine (SVM) based estimation technique is proposed for estimating the bandstop frequency and bandwidth of square-split ring resonators. Artificially engineered surfaces especially the planar frequency selective surfaces like the SRRs have narrowband properties so that estimating the filtering frequencies and the bandwidth is essential in a cost and design-effective way. The proposed method, which is superior to optimization methods and 3D electromagnetic solvers in terms of cost and computational burden, achieved accurate results via SVMs generalization capability. This study represents two SVM regression models one for predicting frequency and the other for predicting bandwidth having fast response and accuracy. Results of the proposed model reveal that resonance frequency estimation error, in terms of percentage, is bounded in the interval [0.0542, 3.5938], with an overall error of 0.89 % for the test data. The mean and standard deviation of the percentage error is obtained as 0.9861 and 0.9376, respectively. In addition to that -10dB bandwidth is estimated with the bounded error where estimation error in terms of percentage would be lie in the interval [0.068925, 6.876800] with an overall error of 3.68% for the test data.

1. INTRODUCTION

Isolating electronic devices is crucial not only in terms of electronic device-to-device interaction but also in terms of protecting the body tissue from electromagnetic pollution. Due to the incredible penetration of electronic devices in our daily life, electromagnetic compatibility became a central issue that can be solved by using additional designs such as frequency selective surfaces (FSS), electronic bandgap structures (EBG), left-handed materials, double negative materials (DNG), single negative materials (SNG), and artificial magnetic conductors (AMC) [1,2,12-20]. FSSs are one of the goal-directed components that researchers pay significant

attention in order with isolation problems [2]. They are periodic arrays of conducting patches or slots on a conducting sheet deposited on a substrate, which behaves as bandpass, and bandstop filters, or absorbers for various frequencies that span up to THz waves from radio waves. Considering the increasingly growing communication systems over the last decades, especially wireless communication allows a striking increase in electromagnetic pollution is on the carpet [1,2]. For all the aforementioned frequency bands restricting unwanted radiation while letting the other signals pass for any system is necessary.

Engineered surfaces are required for filtering the electromagnetic waves and the most familiar one can be regarded as the Split Ring Resonator (SRR) structure. SRR structures, which can be fabricated in different dimensions, are generally fabricated in 2Ds as printed circuit boards by etching the metal element to a dielectric substance. Therefore, an SRR consists of a substrate layer and a patch on the top side of the dielectric substrate. This patch is made of conductive elements, such as gold and copper and they can be designed in several shapes. Due to the advantages in fabrication and implementation, they have received more attention when compared to the 3D versions. Nonetheless, the narrow bandwidth property is an important disadvantage for the proposed structures so that estimating the resonant frequency accurately before manufacturing the design is necessary. Although there are abundant studies performed to find the resonant frequencies in antenna designs, literature is lacking frequency calculation for SRR structures.

Using the 3D electromagnetic solver is one of the most accurate ways to estimate the filtering frequency of the SRR however, the claimer should reconcile the designer to cost, design effort, and computational burden. Another two options, equivalent circuit model and analytical formula for calculating, are cost and time-effective but they are having drawbacks in terms of accuracy. The former is not applicable for higher frequencies since it is not possible to represent such structures with lumped elements at high frequencies and the latter is not accurate because there are no closed-form mathematical expressions for calculating frequency and bandwidth so that optimization will also be a problem due to the lack of mathematical expressions. Among all those techniques for estimating the filtering frequency and bandwidth, Machine Learning (ML) is one of the most preferred ways. Therefore, it is commonly favored by researchers for finding the resonance frequency of RF designs such as antennas. Frequency estimation of FSS is one of the applications that ML can be applied. Supervised and unsupervised learning are the two main approaches that ML can provide. In supervised learning, the aim is to develop a function that maps a set of observations.

In recent years, Support Vector Machine (SVM) applications are becoming more famous and popular in the ML community due to the outstanding performance of the ability of generalization when compared to the traditional methods such as artificial neural network [3-11]. A relatively new supervised non-parametric statistical learning technique, Support vector machines (SVMs), is proposed by Vapnik in 1979 and is based on Vapnik-Chervonenkis theory [3,4]. Therefore, SVM has been implemented into numerous applications such as face detection [3], digit recognition, verification, object detection and recognition, handwritten text detection and categorization [5], speech and speaker verification [6], prediction, etc. Besides those signal applications, it has been used in electromagnetics in microstrip lines [7] and antennas [8,9], filter designs [21], absorber designs [22]. However, to the best of the authors' knowledge, subjects discussing the use of SVM in calculating the properties of SRR are not studied yet.

In this study, a new estimation method is applied to estimate the filtering properties of an S-SRR structure, which is applicable and scalable for several frequency bands. This new estimation technique adopts the SVM regression approach for estimation of the SRR's filtering frequency and -10dB bandwidth by using second-order polynomial kernel and Gaussian kernel-based SVMs respectively, where the minimization problem is solved by utilizing the Sequential Minimization Optimization (SMO) technique. The data set is created by moderate simulate ion runs of 3D EM solver by proposing an SRR structure in 2D geometry. The proposed structure is analyzed in terms of its geometrical and material properties. Impact of substrate thickness, permittivity, copper strip width, slot length, are evaluated regarding the analysis for spanning all possible domains for training. The accuracy of the SVM results is discussed and presented within the paper. SVM approach is conducted considering the filtering frequency f_r and the bandwidth as a function of all those parameters. The results are compared with the 3D solver results and the corresponding error is presented.

2. FREQUENCY AND BANDWIDTH ESTIMATION OF THE S-SRR BY USING SVM

SVM, which is also known as Support Vector Network, used for classification and regression analysis is a good candidate for electromagnetic design problems. Estimating the antenna parameters for a set of training data is one of the application areas in electromagnetics [6-8]. For the given antenna's physical and geometrical parameters, it is possible to estimate antenna operating frequency, bandwidth, and gain parameters. Besides, they are used to estimate the transmission line parameters [7].

In this study, we focused on the frequency and bandwidth estimation of the SRR structure. SVM provides such estimation opportunities in a fast and cost-efficient way. On one hand, considering the full-wave electromagnetic simulators, which are having a burden not only in terms of computation but also in terms of license cost, is a very accurate way of design and optimization. On the other hand, the equivalent circuit model is efficient in terms of cost and quickness. Although equivalent circuit models seem to be a fast model to obtain filtering frequency, it is not an accurate one, especially for high frequencies. Artificial intelligence is getting popular due to its advantages among other methods. As an option ANNs (Artificial Neural Network), which embody traditional empirical Risk Minimization, are candidates for solving such problems; however, they have difficulties in terms of overfitting [10]. On the other hand, a supervised method SVM, which embodies the Structural Risk Minimization principle, are getting popular in the last decades [11]. The generalization capability of SVMs' are superior to ANN is considered in this study and a model is proposed to estimate the band stop frequency and -10dB bandwidth of the square SRR.

Considering a given training data $\{(x_1, y_1) \dots (x_i, y_i)\} \subset \chi \times i$ where i stands for the assembly of real numbers and χ represents the space of input patterns such as $\chi = i^d$ and the goal is to find the function $f(x)$ to approximate the obtained targets y_i for all training data. Here the function $f(x)$ is represented by Lagrange multipliers and Kernel functions, α_i, α_i^* and $K(x_i, x_j)$, respectively as represented in (2.1);

$$f(x) = \sum_{i=1}^{l} (\alpha_i - \alpha_i^*) K \langle x_i, x_j \rangle + b \tag{2.1}$$

where $\langle .,. \rangle$ stands for dot product in χ and b ϵ i and ω ϵ i.

The proposed SVM model approximates the filtering frequencies for the proposed SRR. Those values can be expressed as a function of six SRR parameters as in (2.2) and shown in Figure 1a:

$$f_r = f(x, x_1, w_c, w_s, h_s, \varepsilon_r, h_c) \tag{2.2}$$

Besides the filtering frequency, bandwidth, which is again a function of the structure's physical dimensions and material properties, is crucial in terms of the applications so that it is worth estimating the bandwidth as well as the filtering frequency as in (2.3);

$$BW = g(x, x_1, w_c, w_s, h_s, \varepsilon_r, h_c) \tag{2.3}$$

For performing the estimation, a moderate data set is needed and created by a set of simulations via CST Microwave Studio. The data set is generated by considering all the physical parameters and the material electrical properties and the procedure for the generation of the data set is presented in the next section.

2.1 Data Set Generation

The structure consists of a substrate layer and a patch on the top side of the dielectric substrate having a relative permittivity value of ε_r as shown in Fig. 1a. The side length of the square substrate is denoted as x and the side length of the square SRR is x_1 having a conductor width of w_c and a slot having a width of w_s. The thickness values are h_c and h_s for the conductor and substrate layer, respectively. The resonance frequency of square SRR can be controlled by tuning the capacitance and/or inductance values with the equation $f_r = 1/(2\pi\sqrt{L_{SRR}C_{SRR}})$ where C_{SRR} denoted as the equivalent capacitance and L_{SRR} represent the equivalent inductance values of the SRR. It should be noted that the L_{SRR} and C_{SRR} values, which are depicted in Fig1b, are the functions of several parameters such as, x_1, w_c, w_s, h_s, h_c and ε_r.

In this section, the filtering frequency of the proposed model is evaluated and analyzed according to its physical and geometrical features via a finite-integration based full-wave electromagnetic solver (CST Microwave Studio) having unit cell boundary conditions. The side length of the conductor ring is one of the physical parameters that affect the L_{SRR} value. The larger conductor lengths cause an increment on the equivalent inductance of the SRR, which causes a decrement in filtering frequency value. To observe the characteristic of the frequency response with a variation of the conductor side length, a set of simulations are conducted via CST Microwave Studio, and the impact of the conductor ring's side length (x_1) on the frequency is given in Fig. 2(a). The shorter conductor side length increases the equivalent inductance so that the frequency has created a blueshift in the frequency. Although the side length of the conductor ring increases the equivalent inductance, the width of the conductor (w_c) shows a quite contrary response (cause a redshift in the frequency) since the increment on the conductor width cause a reduction in the equivalent inductance and also reduction in equivalent capacitance value of the circuit model as shown in Fig. (b).
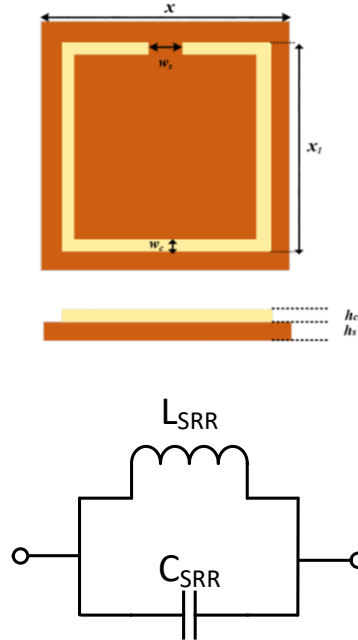
FIGURE 1. Proposed FSS structure (a) geometry (b) equivalent circuit model.

The slot that is created on the conductor loop has a width value of w_s that causes a blueshift with larger values. The variation of the frequency with respect to w_s is presented in Fig. 2(c). Data generation has a set of data regarding the thickness of substrate variation, which can be considered the insignificant effect on filtering bandwidth, but cause a redshift for thicker substrates as presented in Fig. 2(d). The permittivity of the substrate is a parameter that affects the equivalent capacitance where the increase of the permittivity gives a rise in equivalent capacitance of the SRR. Therefore, that frequency decreases with the usage of the high permittivity substrates. The characteristics of the S_{21} with the variation of the permittivity value are given in Fig. 2(e). The Impact of substrate side length (x) is evaluated and the effects are given with the view in Fig. 2(f). It is noteworthy to mention that these changes do not affect the filtering frequency however having a significant effect on bandwidth.
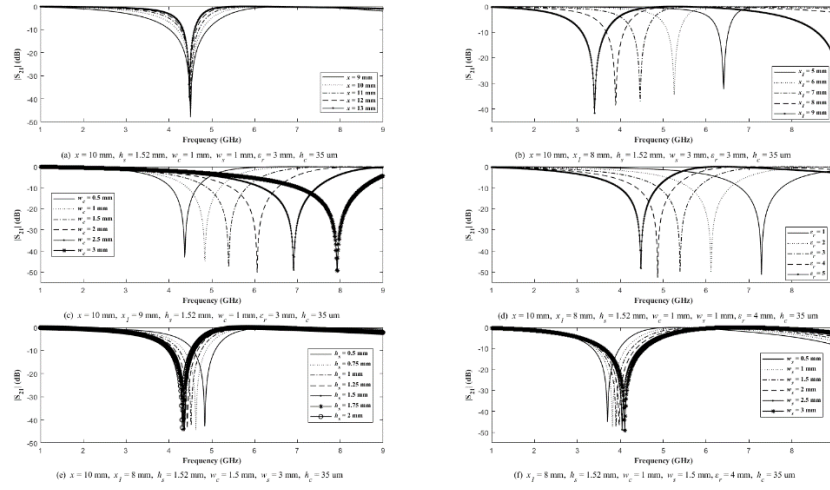
FIGURE 2. Impact of **(a)** conductor ring's side length (x_1), **(b)** conductor width (w_c), **(c)** slot width (w_s), **(d)** substrate thickness (h_s), **(e)** permittivity of the substrate (ε_r), **(f)** substrate side length (x).

2.2 **Adopted SVM For Estimating Filtering Frequency And Bandwidth of SRR**

This study adopts the SVM for estimation of the filtering frequency and -10dB bandwidth of SRR by a polynomial and Gaussian Kernel-based SVM, respectively, which are using SMO (Sequential Minimal Optimization) for solving an optimization problem. The Kernel is a way of computing the dot product of two vectors **x** and **y** in some very high dimensional feature space so that for estimation selecting the kernel type may affect the accuracy directly. Radial basis function kernel (RBF) in other words Gaussian Kernel, which is one of the most popular Kernel Type, is used among linear, polynomial, and Gaussian Kernels for the adoption of the SVM for the problem.

In this study, parameters of the SVM regression model were optimized to obtain the best model for estimating frequency and bandwidth. Optimization studies have been revealed that training SVM by using second-order polynomial kernel function defined in (2.4) gives the best results for the frequency estimation. Crucial parameters, box constraint, kernel scale, and epsilon have been calculated during the optimization process as 177, 15.557, and 0.002829 respectively. A similar study has been carried out for finding out a suitable model for bandwidth estimation. Studies

have been shown that Gaussian kernel-based SVM provides the best results for bandwidth estimation, and box constraint, kernel scale, and epsilon have been calculated as 990.96, 1.1179, and 0.00026873. Gaussian Kernel can be considered as a function whose value depends on the distance from the origin or some point and can be expressed as in (2.4) and (2.5);

$$K(X_1, X_2) = (1 + X_1 X_2)^2 \tag{2.4}$$
$$K(X_1, X_2) = e^{(-\gamma ||X_1 - X_2||^2)} \tag{2.5}$$

Where $||X_1 - X_2||$ stands for Euclidean distance between points X_1 and X_2. Data set consists of frequency and bandwidth responses calculated concerning 1134 different values of 7 parameters, x, x_1, w_c, w_s, w_s h_s, ε_r, and h_c. The commercial substrates have two different copper cladding values the 17 μm and 35 μm. Considering the skin depth value which, shows how deeply an RF signal can penetrate a material, both can be used for the desired frequency interval. Skin depth value which dependents on the frequency as well as the material's properties such as resistivity and permeability where resistivity, f_0 stands for center frequency for the band of interest, μ_r represents the relative permeability and μ_0 represents the free space permeability. The resistivity values for copper, aluminum, gold, silver, and nickel are 1.678 μΩ cm, 2.6548 μΩ cm, 2.24 μΩ cm, 1.586 μΩ cm, and 6.84 μΩ cm, respectively. Considering the cost copper and aluminum, which have a relative permeability value of ≈1, are two of the most preferred cladding conductor in printed technology. Considering the copper skin depth interval is in between 2.06 μm and 0.652 μm for 1GHz and 10 GHz respectively whilst considering the aluminum cladding options those values are in between 2.59 μm and 0.820 μm for the same frequencies. The commercial cladding option, 35 μm is thicker than the skin depth so that the effect of the thickness can be neglected and the input parameters can be considered as 6 as shown in the figure below.
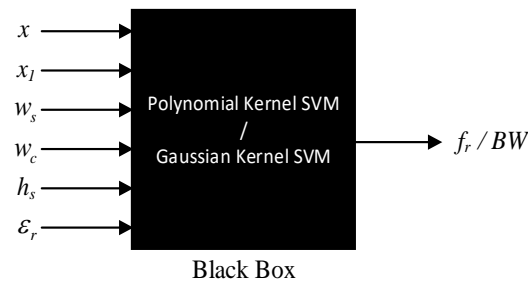

FIGURE 3. SVM illustration as a black box with final input parameters.

Two different SVM regression models have been considered where one of them is for frequency prediction and the other one is for bandwidth prediction. Since the data set is small, both models have been trained by using the whole data set and validation of the SVM regression models has been carried through a k-fold cross-validation procedure. SVM regression models have been tested using new data set generated using a 3D EM solver and frequency and bandwidth predictions obtained by SVM regression models and 3D EM solvers have been compared.

A cross-validation procedure has been performed due to the small training data set. Proposed SVM regression models were validated by performing 5-fold cross-validation by using 1134 sample training data. In this procedure, the training data set is divided into 5 subsets, and one of them is kept as test data and others set to be as training data. SVM regression model is trained using 5 subsets then it is tested using the data hold for the test. This cycle is repeated 5 times where it is guaranteed that each subset is utilized as both test and training data. At each cycle, square error and epsilon loss are calculated and mean values of these parameters are obtained at the end of the validation procedure. Cross-validation results show that the Gaussian kernel-based SVM regression model can be obtained with mean square error 0.00008165 and mean epsilon loss 0.0051172. On the other hand, a second-order polynomial kernel-based SVM regression model can be obtained with a mean square error of 0.04703 and mean epsilon loss of 0.085467.

All the simulations have been performed on Dell Precision Tower 7810 workstation with 10 CPU cores and 32GB RAM. Training phases of Gaussian kernel-based SVN and second-order polynomial kernel-based SVN took 25.23s and 0.81s, respectively.

3. Results And Discussion

Frequency estimation results presented in Table 1 shows that frequency estimations obtained using the SVM regression model are consistent with the frequencies obtained from the 3D EM solver. Results also reveal that resonance frequency estimation error, in terms of percentage, is bounded in the interval [0.0542, 3.5938], which corresponds to a frequency estimation 144MHz above the true resonance frequency in the worst case. The mean and standard deviation of the percentage error is obtained 0.9861 and 0.9376, respectively. Frequency values belonging to test data and estimated by the SVM regression model have been depicted in Fig.4a. Both frequency estimation error percentages and the results given in Fig. 4a show that the proposed second-order polynomial kernel function-based SVM regression model is a good candidate for the resonance frequency estimation in the SRR having an overall error of 0.89% for 27 different test data given in the table below.

In Table 2, -10dB bandwidth results of the 3D EM solver and SVM regression model have been presented. f_l and f_u represent the upper and lower frequency by which the bandwidth region is defined. A similar discussion can be made for the results presented in Table 2. Bandwidth estimations with the SVM regression model are also consistent with the 3D EM solver results. However, the bandwidth estimation error is greater than the errors obtained in the frequency estimation problem. Since the number of parameters affecting bandwidth is less than those that affect the frequency and we used the same training data set to train the SVM model, the non-informative redundant part of the training data has led to being represented bandwidth with less accuracy. In other words, a small part of the training data set contains information about the relation between design parameters and bandwidth. As a result, it is possible to get more accurate results by changing or expanding the training data set. Bandwidth estimation results are presented in Table 2 and Fig. 4b. Results show that -10dB bandwidth can be estimated with the bounded error where estimation error in terms of percentage would be lie in the interval [0.068925, 6.8768]. Furthermore, the mean and standard deviation of the error percentage has been obtained 3.6828 and 1.8932, respectively. In the worst case, results reveal that bandwidth was being estimated at 105.1 MHz less than the true bandwidth reported by the 3D EM solver. The estimation of bandwidth is conducted with an overall error of 3.68% for the given test data.

TABLE 1. Filtering frequency comparison with 3D EM solver and SVM (units of the dimensions are in mm and frequencies and bandwidths in GHz).

| Structural Parameters of Square SRR | | | | | | | Frequency | | Error % |
x	x_1	w_c	w_s	h_s	ε_r	h_c	3D EM solver	SVM	
10	8	1.5	3	1.52	1	0.035	7.310	7.2057	1.4265
10	8	1.5	3	1.52	2	0.035	6.116	6.1698	0.8801
10	8	1.5	3	1.52	3	0.035	5.386	5.3949	0.1657
10	8	1.5	3	1.52	4	0.035	4.885	4.8810	0.0813
10	8	1.5	3	1.52	5	0.035	4.475	4.6281	3.422
12	8.5	1.5	3	1.52	3	0.035	4.177	6.7159	2.4709
12	9	1.5	3	1.52	3	0.035	3.925	5.6368	1.0001
12	9.5	1.5	3	1.52	3	0.035	3.682	4.7508	1.1014
12	10	1.5	3	1.52	3	0.035	3.475	4.0577	0.4986
12	10.5	1.5	3	1.52	3	0.035	3.277	6.6142	1.3523
12	11	1.5	3	1.52	3	0.035	8.218	6.0082	1.5935
10	8	1	1.5	1.6	3	0.035	4.492	5.4505	0.916
10	8	1	1.5	1.7	3	0.035	4.483	4.9410	0.7442
10	8	1	1.5	1.8	3	0.035	4.465	4.4797	2.4248

10	8	1	1.5	1.9	3	0.035	4.447	4.4952	0.0702
10	8	1	1.5	2.0	3	0.035	4.438	4.4636	0.4318
10	8	1	1.5	1.52	3	0.035	4.510	4.4349	0.6739
10.5	8	1	1.5	1.52	3	0.035	4.501	4.4090	0.8556
11	8	1	1.5	1.52	3	0.035	4.501	4.3858	1.1768
11.5	8	1	1.5	1.52	3	0.035	4.492	4.5224	0.2741
12	8	1	1.5	1.52	3	0.035	4.483	4.4974	0.0804
10	8	0.5	3	1.52	3	0.035	4.366	4.4813	0.4387
10	8	1.0	3	1.52	3	0.035	4.843	4.4740	0.4011
10	8	1.5	3	1.52	3	0.035	5.392	4.4756	0.1658
10	8	2.0	3	1.52	3	0.035	6.076	4.3291	0.8458
10	8	2.5	3	1.52	3	0.035	6.922	4.8186	0.5043
10	8	3.0	3	1.52	3	0.035	7.93	5.3949	0.0542

TABLE 2. Bandwidth comparison with 3D EM solver and SVM (units of the dimensions are in mm and frequencies and bandwidths in GHz).

Structural Parameters of Square SRR									BW		Error %
x	x_1	w_c	w_s	h_s	ε_r	h_c	f_l	f_u	3D EM solver	SVM	
10	8	1.5	3	1.52	1	0.035	6.807	7.766	0.958	0.9108	4.925
10	8	1.5	3	1.52	2	0.035	5.616	6.548	0.932	0.8811	5.4603
10	8	1.5	3	1.52	3	0.035	4.889	5.807	0.918	0.8725	4.9559
10	8	1.5	3	1.52	4	0.035	4.3812	5.26	0.882	0.845	4.1905
10	8	1.5	3	1.52	5	0.035	3.979	4.864	0.885	0.838	5.3121
10	5.5	1	1	1.52	3	0.035	6.706	7.039	0.333	0.3402	2.1764
10	6.5	1	1	1.52	3	0.035	5.383	5.752	0.369	0.3837	3.9869
10	7.5	1	1	1.52	3	0.035	4.456	4.897	0.441	0.4672	5.9518
10	8.5	1	1	1.52	3	0.035	3.772	4.339	0.567	0.5509	2.8396
12	7	1.5	3	1.52	3	0.035	6.265	6.751	0.486	0.5168	6.333
12	7.5	1.5	3	1.52	3	0.035	5.653	6.148	0.495	0.5115	3.3246
12	8	1.5	3	1.52	3	0.035	5.122	5.635	0.513	0.5126	0.0689
12	8.5	1.5	3	1.52	3	0.035	4.690	5.230	0.540	0.5227	3.2124
12	9	1.5	3	1.52	3	0.035	4.294	4.852	0.558	0.5333	4.4216
10	8	1	1.5	1.6	3	0.035	4.195	4.744	0.549	0.5554	1.169
10	8	1	1.5	1.7	3	0.035	4.177	4.735	0.558	0.5559	0.381
10	8	1	1.5	1.8	3	0.035	4.717	4.168	0.549	0.5574	1.5266
10	8	1	1.5	1.9	3	0.035	4.699	4.150	0.549	0.5589	1.8084
10	8	1	1.5	2.0	3	0.035	4.690	4.141	0.549	0.5583	1.6926

| 10	8	1	1.5	1.52	3	0.035	4.197	4.781	0.585	0.5558	4.991
10.5	8	1	1.5	1.52	3	0.035	4.726	4.249	0.477	0.4975	4.3045
11	8	1	1.5	1.52	3	0.035	4.261	4.696	0.435	0.4112	5.4603
11.5	8	1	1.5	1.52	3	0.035	4.654	4.294	0.360	0.3398	5.6173
12	8	1	1.5	1.52	3	0.035	4.298	4.638	0.340	0.3242	4.6402
10	8	0.5	3	1.52	3	0.035	4.033	4.660	0.627	0.5931	5.4016
10	8	1.0	3	1.52	3	0.035	4.431	5.174	0.743	0.7289	1.9044
10	8	1.5	3	1.52	3	0.035	4.901	5.785	0.884	0.8725	1.3003
10	8	2.0	3	1.52	3	0.035	5.480	6.542	1.062	1.0145	4.4726
10	8	2.5	3	1.52	3	0.035	6.207	7.442	1.234	1.2123	1.7772
10	8	3.0	3	1.52	3	0.035	7.009	8.538	1.528	1.4229	6.8768
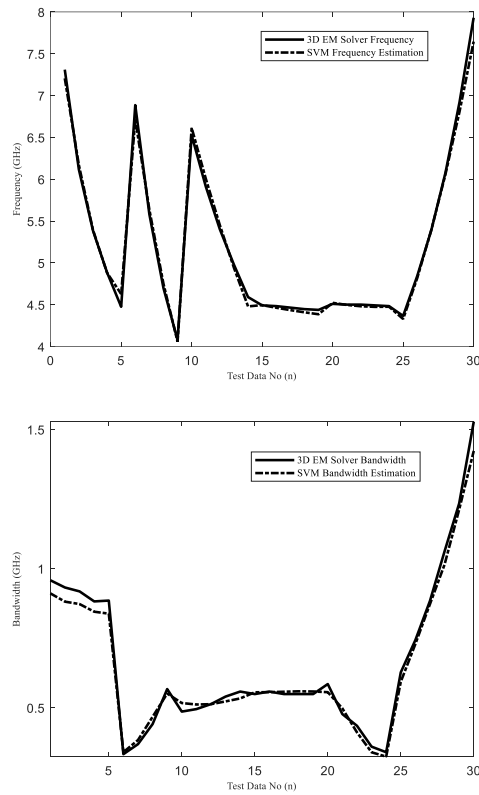
FIGURE 4. SVM and 3D solver comparison for (a) frequency (b) bandwidth.

5. Conclusions

Results showed that the SVM technique for estimating frequency and bandwidth is preferable due to its generalization capability, fast response, and accuracy. The technique has advantages when compared to 3D electromagnetic solvers, optimization, and other artificial intelligence techniques in terms of license cost, computational burden, and risk minimization. It should be noted that a very good consistency has been achieved in terms of stopband and bandwidth between the 3D solver and SVM regression model by using moderate training data set created via 3D full-wave electromagnetic simulations.

Author Contribution Statements Authors are equally contributed to the paper. All authors read and approved the final copy of the manuscript.

Declaration of Competing Interests The authors declare that they have no known competing financial interests or personal relationships that could have appeared to influence the work reported in this paper.

References

[1] Can, S., Yilmaz, A.E., Reduction of specific absorption rate with artificial magnetic conductors, *Int. J. RF Microw. Comput. Aided Eng.,* 26 (4) (2016), 349-354. https://doi.org/10.1002/mmce.20974

[2] Munk, B.A., Frequency Selective Surfaces: Theory and Design, John Wiley & Sons Inc., New York, 2000.

[3] Vapnik, V.N., The Nature of Statistical Learning Theory, Springer-Verlag, New York, 1995.

[4] Tsai, H.H., Chang, Y.C., Facial expression recognition using a combination of multiple facial features and support vector machine. *Soft Comput.*, 22 (2018), 4389-4405. https://doi.org/10.1007/s00500-017-2634-3

[5] Aly, S., Mohamed, A., Unknown-length handwritten numeral string recognition using cascade of PCA-SVMNet classifiers, *IEEE Access*, 7 (2019), 52024-52034. https://doi.org/10.1109/ACCESS.2019.2911851

[6] Yaman, S., Pelecanos, J., Using polynomial kernel support vector machines for speaker verification, *IEEE Signal Process. Lett.*, 20 (9) (2013), 901-904. https://doi.org/10.1109/LSP.2013.2273127

[7] Gunes, F., Tokan, N.T., Gurgen, F., Support vector design of the microstrip lines, *Int. J. RF Microw. Comput. Aided Eng.*, 18 (2008), 326-336. https://doi.org/10.1002/mmce.20290

[8] Zheng, Z., Chen, X., Huang, K., Application of support vector machines to the antenna design, *Int. J. RF Microw. Comput. Aided Eng.,* 21 (1) (2011), 85–90. https://doi.org/10.1002/mmce.20491

[9] El Misilmani, H.M., Naous, T., Al Khatib, S.K., A review on the design and optimization of antennas using machine learning algorithms and techniques*, Int. J. RF Microw. Comput. Aided Eng.*, 30 (2020), 22356. https://doi.org/10.1002/mmce.22356

[10] Gunn, S.R., Support vector machines for classification and regression, *SISI Tech. Reports*, 6459, 1998.

[11] Cortes, C., Vapnik, V.N., Support vector networks, *Mach. L.,* 20 (1997), 73-297.

[12] Yilmaz, A.E., Kuzuoglu, M., Design of the square loop frequency selective surfaces with particle swarm optimization via the equivalent circuit model, Radioengineering, 18 (2) (2009), 95-102.

[13] Li, J., Li, Y., Cen,Y., Zhang, C., Luo, T., Yang, D., Applications of neural networks for spectrum prediction and inverse design in the terahertz band, *IEEE Photonics J.,* 12 (5) (2020),1-9. https://doi.org/10.1109/JPHOT.2020.3022053

[14] Qiu, T., Deep learning: a rapid and efficient route to automatic metasurface design, Adv. Sci. Lett., 6 (12) (2019), 1900128. https://doi.org/ 10.1002/advs.201900128

[15] Alcantara Neto, M.C.A, Oeiras Ferreira, H.R., Leite de Araújo, J.P., Brito Barros F.J., Gomes Neto, A., Oliveira Alencar, M., dos Santos Cavalcante, G.P., Compact ultra-wideband FSS optimized through fast and accurate hybrid bio-inspired multi objective technique, IET Microwaves, *Antennas & Propag.*, 14 (2020), 884-890. https://doi.org/ 10.1049/iet-map.2019.0821

[16] Chaudhary, V., Panwar, R., FSS Derived Using a New Equivalent Circuit Model Backed Deep Neural Network., *IEEE Antennas Wirel. Propag. Lett.,* 20 (10) (2021), 1963-1967. https://doi.org/ 10.1109/LAWP.2021.3101225

[17] Bozzi, M., Manara, G., Monorchio, A., Perregrini, L., Automatic design of inductive FSSs using the genetic algorithm and the MoM/BI-RME analysis, *IEEE Antennas Wirel. Propag. Lett.,* 1 (2002), 91-93. https://doi.org/10.1109/LAWP.2002.805129

[18] Chakravarty, S., Mittra, R., Design of a frequency selective surface (FSS) with very low cross-polarization discrimination via the parallel micro-genetic algorithm (PMGA), *IEEE Trans. Antennas Propag.*, 51 (7) (2003), 1664-1668. https://doi.org/ 10.1109/TAP.2003.813637

[19] Zhu, D.Z., Werner, P.L., Werner, D.H., Design and optimization of 3-D frequency-selective surfaces based on a multi objective lazy ant colony optimization algorithm, *IEEE Trans. Antennas Propag.*, 65 (12) (2017), 7137-7149. https://doi.org/10.1109/TAP.2017.2766660

[20] Ohira, M., Deguchi, H., Tsuji, M., Shigesawa, H. Multiband single-layer frequency selective surface designed by combination of genetic algorithm and geometry-refinement technique, *IEEE Trans. Antennas Propag.*, 52 (11) (2004), 2925-2931. https://doi.org/10.1109/TAP.2004.835289

[21] Monorchio, A., Manara, G., Serra, U., Marola, G., Pagana, E., Design of waveguide filters by using genetically optimized frequency selective surfaces., *IEEE Microw. Wirel. Compon. Lett.*, 15 (6) (2005), 407-409. https://doi.org/10.1109/LMWC.2005.850482

[22] Cui, S., Weile, D.S., Volakis, J.L., Novel planar electromagnetic absorber designs using genetic algorithms., *IEEE Trans. Antennas Propag.,* 54 (6) (2006), 1811-1817. https://doi.org/10.1109/TAP.2006.875460

INSTRUCTIONS TO CONTRIBUTORS

Communications Faculty of Sciences University of Ankara Series A2-A3: Physical Sciences and Engineering is a single-blind peer reviewed open access journal which has been published since 1948 by Ankara University, accepts original research articles written in English in the fields of Physics, Engineering Physics, Electronics/Computer Engineering, Astronomy and Geophysics. Review articles written by eminent scientists can also be invited by the Editor.

Article-processing charges: The publication costs for Communications Faculty of Sciences University of Ankara Series A2-A3: Physical Sciences and Engineering are covered by the journal, so authors do not need to pay an article-processing and submission charges. The PDF copies of accepted papers are free of charges and can be downloaded from the webside. Hard copies of the paper, if required, are due to be charged for the amount of which is determined by the administration each year.

Submission: All manuscripts should be submitted via our online submission: https://dergipark.org.tr/en/journal/2457/submission/step/manuscript/new Note that only two submissions per author per year will be considered. Once a paper is submitted to our journal, all co-authors need to wait 6 months from the submission date before submitting another paper.

Cover Letter: Manuscripts should be submitted in the PDF form used in the peer-review process together with THE COVER LETTER and the source file (Supporting File). In the cover letter the authors should suggest the most appropriate Area Editor for the manuscript and potential four reviewers with full names, universities and institutional email addresses. Proposed reviewers must be experienced researchers in your area of research and at least two of them should be from different countries. In addition, proposed reviewers must not be co-auhors, advisors, students, etc. of the authors. In the cover letter, the author may enter the name of anyone who he/she would prefer not to review the manuscript, with detailed explanation of the reason. Note that the editorial office may not use these nominations, but this may help to speed up the selection of appropriate reviewers.

Preparing your manuscript: Manuscripts should be typeset using as a DOC file. Authors will submit their manuscript and the cover letter via our submission system. A template of manuscript can be reviewed in https://dergipark.org.tr/tr/download/journal-file/20554 (or can be reviewed in pdf form).

Title Page: The title page should contain the title of the paper, full names of the authors, affiliations addresses and e-mail addresses of all authors. Authors are also required to submit their Open Researcher and Contributor ID (ORCID)'s which can be obtained from http://orcid.org as their URL address in the format http://orcid.org/xxxx-xxxx-xxxx-xxxx. Please indicate the corresponding author.

Abstract and Keywords: The abstract should state briefly the purpose of the research. The length of the Abstract should be between 50 to 5000 characters. At least 3 keywords are required.

Math Formulae: Formulas should be numbered consecutively in the parentheses ( ).

Tables: All tables must have numbers (TABLE 1) consecutively in accordance with their appearance in the text and a legend above the table. Please submit tables as editable text not as images.

Figures: All figures must have numbers (FIGURE 1) consecutively in accordance with their appearance in the text and a caption (not on the figure itself) below the figure. Please submit figures as EPS, TIFF or JPEG format.

Authors Contribution Statement, Declaration of Competing Interests and Acknowledgements should be given at the end of the article before the references.

References: The following format for the references should be used. Authors are urged to use the Communication.csl style (https://dergipark.org.tr/en/download/journal-file/18514) in Mendeley Desktop or Zotero automated bibliography. If manual entry is prefered for bibliography, then all citations must be listed in the references part and vice versa. Below, It has no relationship with the text, but can be used to show sample citations such as; for articles [1, 4], for books/booklets/theses [3], and for proceedings/conferences etc. [2].

[1] Demirci, E., Unal, A., Özalp, N., A fractional order SEIR model with density dependent death rate, Hacettepe J. Math. Stat., 40 (2) (2011), 287–295.

[2] Gairola, A. R., Deepmala, Mishra, L. N., Rate of approximation by finite iterates of q-Durrmeyer operators, Proc. Natl. Acad. Sci. India Sect. A Phys. Sci., 86 (2) (2016), 229–234.

[3] Lehmann, E. L., Casella, G., Theory of Point Estimation, Springer, New York, 2003.

[4] Özalp, N., Demirci, E., A fractional order SEIR model with vertical transmission, Math. Comput. Model., 54 (1-2) (2011), 1–6. https://dx.doi.org/10.1016/j.mcm.2010.12.051

Peer-review policy: The Editor may seek the advice of two, or three referees, depending on the response of the referees, chosen in consultation with appropriate members of the Editorial Board, from among experts in the field of specialization of the paper. The reviewing process is conducted in strict confidence and the identity of a referee is not disclosed to the authors at any point since we use a single-blind peer review process.

Copyright: Copyright on any open access article in Communications Faculty of Sciences University of Ankara Series A2-A3: Physical Sciences and Engineering is licensed under a Creative Commons Attribution 4.0 International License (CC BY).

Declarations/Ethics With the submission of the manuscript authors declare that:

- All authors of the submitted research paper have directly participated in the planning, execution, or analysis of study;
- All authors of the paper have read and approved the final version submitted;
- The contents of the manuscript have not been submitted, copyrighted or published elsewhere and the visual-graphical materials such as photograph, drawing, picture, and document within the article do not have any copyright issue;
- The contents of the manuscript will not be copyrighted, submitted, or published elsewhere, while acceptance by the Journal is under consideration.
- The article is clean in terms of 'plagiarism', and the legal and ethical responsibility of the article belong to the author(s). Author(s) also accept that the manuscript may go through plagiarism check using IThenticate software;
- The objectivity and transparency in research, and the principles of ethical and professional conduct have been followed. Authors have also declared that they have no potential conflict of interest (financial or non-financial), and their research does not involve any human participants and/or animals.

Archiving: Research papers published in Communications Faculty of Sciences University of Ankara are archived in the Library of Ankara University (Volume 1-60) and Dergipark immediately following publication with no embargo.

Editor in Chief
Commun. Fac. Sci. Univ. Ank. Ser. A2-A3.
Ankara University, Faculty of Sciences
06100, Besevler - ANKARA TURKEY

C O M M U N I C A T I O N S